A point mutation in the nucleotide exchange factor eIF2B constitutively activates the integrated stress response by allosteric modulation

Morgane Boone[1,2#], Lan Wang[1,2,#], Rosalie E Lawrence[1,2], Adam Frost[2,3], Peter Walter[1,2,*], Michael Schoof[1,2*]

Affiliations

[1]Howard Hughes Medical Institute, University of California at San Francisco, San Francisco, CA, USA.

[2]Department of Biochemistry and Biophysics, University of California at San Francisco, San Francisco, CA, USA.

[3]Chan Zuckerberg Biohub, San Francisco, CA, USA.

[#] These authors contributed equally

* To whom correspondence should be addressed; Email: Peter@walterlab.ucsf.edu, michael@walterlab.ucsf.edu

Abstract

In eukaryotic cells, stressors reprogram the cellular proteome by activating the integrated stress response (ISR). In its canonical form, stress-sensing kinases phosphorylate the eukaryotic translation initiation factor eIF2 (eIF2-P), which ultimately leads to reduced levels of ternary complex required for initiation of mRNA translation. Previously we showed that translational control is primarily exerted through a conformational switch in eIF2's nucleotide exchange factor, eIF2B, which shifts from its active A-State conformation to its inhibited I-State conformation upon eIF2-P binding, resulting in reduced nucleotide exchange on eIF2 (Schoof et al. 2021). Here, we show functionally and structurally how a single histidine to aspartate point mutation in eIF2B's β subunit (H160D) mimics the effects of eIF2-P binding by promoting an I-State like conformation, resulting in eIF2-P independent activation of the ISR. These findings corroborate our previously proposed A/I-State model of allosteric ISR regulation.

Introduction

Coping with cellular stressors, manifesting as either intrinsic cues or environmental insults, is key to preserving cellular and organismal health. One strategy is to activate the integrated stress response (ISR), a conserved eukaryotic signaling network that reprograms translation towards damage mitigation and recovery, or apoptosis when stress is irremediable (Costa-Mattioli and Walter 2020). The ISR integrates diverse stresses through at least four stress-sensing kinases – PERK, HRI, GCN2, PKR, and perhaps MARK2, via phosphorylation of a single serine, S51 of the α subunit of the translation initiation factor eIF2 (Hinnebusch 2005; Guo et al. 2020; Dey et al. 2005; Shi et al. 1998; Lu et al. 2021). eIF2 is a central player in translation initiation, mediating start codon recognition on the mRNA and delivery of the initiator methionine tRNA. Phosphorylation of eIF2 disrupts this process and leads to a precipitous drop in global protein synthesis. Conversely, the translation of a subset of stress-responsive mRNAs, such as *ATF4*, generally repressed by the presence of 5' UTR upstream open reading frames (uORFs), is induced (Harding et al. 2000). The alternative translation program that is thus set in motion drives the cell's return to homeostasis. While the ISR is inherently cytoprotective, its dysregulation has been documented in multiple disease states. Specifically, the ISR has been linked to neurodegenerative diseases (Ma et al. 2013), brain-injury induced dementia (Chou et al. 2017; Sen et al. 2017), aging (Krukowski et al. 2020), diabetes (Abdulkarim et al. 2015; Harding et al. 2001), and cancer (Nguyen et al. 2018; Koromilas et al. 1992).

Mechanistically, it is the level of ternary complex (TC) that determines the regulation of translation initiation by the ISR. The TC consists of eIF2 (heterotrimer composed of an α, β, and γ subunit, containing a GTPase domain in its γ subunit), the initiator tRNA loaded with methionine (Met-tRNA^{i}), and GTP (Algire, Maag, and Lorsch 2005). Once the TC associates with the 40S ribosomal subunit, additional initiation factors, and the 5' methylguanine cap of the mRNA, the pre-initiation complex scans the mRNA for a start codon. Recognition of the start codon leads to GTP hydrolysis and triggers the release of eIF2 now bound to GDP (as reviewed in (Hinnebusch, Ivanov, and Sonenberg 2016)). The large ribosomal subunit joins and the assembled 80S ribosome proceeds with elongation of the polypeptide chain. Crucially, for every round of cap-dependent translation initiation, eIF2 requires GDP-to-GTP exchange, catalyzed by its dedicated

66 guanine nucleotide exchange factor (GEF), eIF2B. Failure to complete this step impacts
67 the cellular concentration of the TC, which impairs the translation of most mRNAs. At the
68 same time, lower TC concentrations can induce the translation of specific stress-
69 responsive ORFs, some of which are regulated by uORFs (Harding et al. 2000; Lu,
70 Harding, and Ron 2004; Vattem and Wek 2004). Thus, the ISR regulates translation by
71 tuning the available pool of TC.
72
73 Given its central role in controlling TC levels and mRNA translation, many eIF2B
74 mutations result in an aberrant ISR and severe disease, such as Vanishing White Matter
75 Disease (VWMD) (Leegwater et al. 2001; van der Knaap et al. 2002). Molecularly, eIF2B
76 is a large, heterodecameric complex composed of two copies each of an α, β, γ, δ, and ε
77 subunit (Kashiwagi et al. 2016; Tsai et al. 2018; Zyryanova et al. 2018; Wortham et al.
78 2014; Gordiyenko et al. 2014). It has long been established that phosphorylation of eIF2
79 (eIF2-P) converts eIF2 from an eIF2B substrate to an eIF2B inhibitor, leading to a
80 reduction in GEF activity and ISR activation (Siekierka, Mauser, and Ochoa 1982; Matts,
81 Levin, and London 1983; Konieczny and Safer 1983; Salimans et al. 1984; Rowlands,
82 Panniers, and Henshaw 1988). Earlier atomic-resolution snapshots of the eIF2-bound
83 and eIF2-P-bound human eIF2B complexes suggested steric hindrance to be the
84 predominant mechanism for inhibition, given the proposed overlap of binding sites
85 (Kenner et al. 2019; Kashiwagi et al. 2019; Adomavicius et al. 2019; Gordiyenko, Llácer,
86 and Ramakrishnan 2019; Bogorad, Lin, and Marintchev 2017). However, we and others
87 recently discovered that binding of the inhibitor eIF2-P to a distinct binding site —
88 located on the face of the eIF2B complex opposite of the substrate-binding site —
89 allosterically switches eIF2B from its active 'A-State' (which can readily engage eIF2 and
90 catalyze nucleotide exchange) to an inhibited 'I-State' (Schoof et al. 2021; Zyryanova et
91 al. 2021).
92
93 The multi-subunit composition of eIF2B also lends itself to regulation at the level of
94 complex assembly. The decameric holoenzyme is built from two eIF2Bβγδε tetramers
95 and one eIF2Bα_2 dimer (Tsai et al. 2018). The eIF2Bε subunit harbors the enzyme's
96 catalytic center but only contains a small part of the binding surface of eIF2. Two of four
97 interfaces between eIF2 and eIF2B (IF1 and IF2) reside in eIF2Bε. Thus, poor substrate-
98 binding severely limits eIF2Bε's catalytic activity. The substrate-binding surface is
99 increased upon addition of more subunits (a third interface, IF3 in eIF2Bβ). Yet, even

when embedded in the eIF2Bβγδε tetramer subcomplex, the specific enzyme activity (k_{cat}/K_M) of eIF2Bε is ~100-fold lower compared to the fully assembled eIF2B$(\alpha\beta\gamma\delta\varepsilon)_2$ decamer (tetramer k_{cat}/K_M = 0.07 $min^{-1}\mu M^{-1}$, decamer k_{cat}/K_M = 7.24 $min^{-1}\mu M^{-1}$), in which the substrate-interacting surface is further extended by bridging the two-fold symmetric interface formed between the two tetrameric subcomplexes (a fourth interface, IF4 in eIF2Bδ') (Schoof et al. 2021; Kenner et al. 2019; Kashiwagi et al. 2019).

eIF2B activity, assembly-state, and conformation are all modulated by the ISR inhibitor, ISRIB. This small molecule binds in a deep groove spanning across the symmetry interface of the two eIF2B tetramers and enhances its GEF activity (Sekine et al. 2015; Sidrauski et al. 2013; Sidrauski et al. 2015; Tsai et al. 2018; Zyryanova et al. 2018). ISRIB exerts these effects by acting on both eIF2B assembly and conformation (Schoof et al. 2021). When eIF2Bα_2 levels are low, pharmacological dimerization of tetrameric subcomplexes by ISRIB rescues eIF2B function (Schoof et al. 2021). When eIF2Bα_2 levels are saturating and eIF2B decamers are therefore fully assembled, ISRIB binding stabilizes eIF2B in the active 'A-State', reducing its affinity for the inhibitor eIF2-P (Schoof et al. 2021; Zyryanova et al. 2021).

Given these insights, we here revisit previous observations concerning a histidine to aspartate point mutation in eIF2Bβ (βH160D) that straddles the junction of the β-β'and β-δ' interface (the ' notation indicates that the subunit resides in the adjoining, second tetramer in eIF2B) (Tsai et al. 2018). We formerly observed that this missense mutation blocked ISRIB-driven assembly of eIF2B tetramers into octamers *in vitro*, underlining the importance of the H160 residue in stabilizing the octamer (Tsai et al. 2018). However, whether the change to aspartic acid, predicted to be repulsed by the apposed D450 in δ', precluded decameric assembly or activated the ISR, remained unknown. Here, we show that the βH160D mutation does not affect decameric holoenzyme formation when all subunits are present. However, this mutation stabilizes eIF2B in an inactive conformation reminiscent of the inhibited 'I-State', normally promoted by eIF2-P binding. Concomitantly, cells with this mutation constitutively activate the ISR, even in absence of stress and eIF2-P. These results validate the A/I-State model of eIF2B and ISR regulation by showing that a conformational change in eIF2B is sufficient to impair its enzymatic function and activate the ISR.

Results

The eIF2B βH160D mutation does not block decamer assembly *in vitro*

To dissect the regulation of eIF2B assembly and activity, we purified human eIF2Bβδγε tetramers both with and without the βH160D mutation (Figure 1 – figure supplement 1). We first performed sedimentation velocity experiments to assess the assembly state of eIF2B. Consistent with our previous observations (Tsai et al. 2018), WT eIF2B tetramers readily assembled into octamers in the presence of ISRIB, whereas βH160D tetramers did not (Figure 1A-B). In contrast, we found that assembly into the fully decameric holoenzyme by addition of the eIF2Bα_2 dimer was not compromised (Figure 1C-D).

To confirm that the βH160D mutation does not impair decamer assembly, we utilized an orthogonal, previously established Förster resonance energy transfer (FRET) assay to assess eIF2B's assembly state (Schoof et al. 2021). In this system, the C-terminus of eIF2Bβ is tagged with mNeonGreen as the FRET donor and the C-terminus of eIF2Bδ with mScarlet-i as the FRET acceptor. Both WT and βH160D tetramers were purified with these fluorescent tags (and hereafter are denoted eIF2Bβδγε-F). A titration of ISRIB readily assembled WT eIF2Bβδγε-F tetramers into octamers (EC_{50} = 170 ± 25 nM) but did not promote βH160D eIF2Bβδγε-F assembly into octamers , even at the highest concentrations tested (Figure 1E). By contrast and in agreement with the analytical ultracentrifugation data in Figure 1A-D, titration of eIF2Bα_2 assembled both WT (EC_{50} = 29 ± 3 nM) and βH160D (EC_{50} = 33 ± 3 nM) eIF2Bβδγε-F tetramers into decamers with comparable efficiency (Figure 1F).

The eIF2B βH160D decamer is impaired in GEF activity

These properties are reminiscent of eIF2B's behavior in the presence of its inhibitor eIF2-P. In the inhibited decameric conformation (I-State) induced by eIF2-P binding, ISRIB binding to eIF2B is impaired (Schoof et al. 2021; Zyryanova et al. 2021). We next asked whether the βH160D mutation impacts eIF2B's enzymatic activity. To this end, we monitored eIF2B's GEF activity using a BODIPY-FL-GDP nucleotide exchange assay. Both WT and βH160D tetramers exhibited comparably low enzymatic activity. The activity was robustly enhanced in WT octamers assembled from tetramers with ISRIB but, as expected, ISRIB had no impact on βH160D tetramer activity (Figure 2A). Intriguingly, βH160D decamers were less active than WT decamers ($t_{1/2}$ = 23.6 ± 0.8

min vs. 9.3 ± 1.0 min, respectively) (Figure 2B). To understand how the βH160D mutation impaired eIF2B's GEF activity, we next performed nucleotide exchange assays of WT and βH160D decamer activity at varying eIF2 concentrations. We measured the initial velocity of these reactions and fit the data to the Michaelis-Menten model of enzyme kinetics to determine the V_{max} and the K_M of the nucleotide loading reaction (Figure 2C, Figure 2 – figure supplement 1). The V_{max} (and consequently also the k_{cat}) was significantly diminished by ~three-fold for βH160D decamers when compared to WT decamers (WT V_{max} = 1.86 ± 0.13 pmol / min; βH160D V_{max} = 0.66 ± 0.03 pmol / min, two-sided t-test p = 0.0045) suggesting that the βH160D mutation limits the intrinsic enzymatic activity of eIF2B (Figure 2D). In contrast, we could not detect a significant difference in measured K_M (WT K_M = 0.36 ± 0.06 μM, βH160D K_M = 0.19 ± 0.04 μM, two-sided t-test p = 0.07).

Impaired substrate binding in decameric eIF2B results from the βH160D mutation

The absence of a clear difference in K_M was puzzling, as we suspected the βH160D decamer to adopt an inhibited conformation reminiscent of the I-State, where both intrinsic enzymatic activity and binding of eIF2 are compromised (Schoof et al. 2021). We therefore directly assessed binding affinities of eIF2B's substrate (eIF2) and inhibitor (eIF2-P), using surface plasmon resonance (SPR) to measure binding to WT decamers, βH160D decamers, and WT tetramers. eIF2 association with WT and βH160D decamers was monophasic, but dissociation was notably biphasic irrespective of eIF2 concentration, with a fast phase and a slow phase (Figure 3A-B). Although the rate constants k_a, $k_{d\ fast}$, and $k_{d\ slow}$ were broadly comparable, eIF2 binding to WT vs. βH160D decamers differed in the percentage of fast phase dissociation events (WT = 29%; βH160D = 67%) (Figure 3A-B, Table 1). Thus, a larger fraction of substrate molecules dissociates rapidly from βH160D compared to WT decamers. Since the K_M is only equal to the K_D when the dissociation rate constant k_d is much larger than the k_{cat}, this measurement can resolve the paradox of a similar K_M but different dissociation behavior.

In contrast to eIF2's interaction with decameric eIF2B, binding to WT tetramers could be modeled using one phase association and dissociation. Indeed, eIF2 dissociation from tetrameric eIF2B can be thought of as being 100% fast phase as the dissociation constant was indistinguishable from the fast phase dissociation constant for both WT and βH160D (k_d = 0.12 s^{-1}) (Figure 3C). The fraction of eIF2 molecules that dissociate

from decamers with fast phase kinetics may therefore only be engaging eIF2B through interfaces 1-3 (interfaces 1 and 2 in eIF2Bε and interface 3 in eIF2Bβ). In contrast, the eIF2 molecules that dissociate with slow phase kinetics may additionally contact interface 4 in eIF2Bδ', reaching across the central symmetry interface (Schoof et al. 2021). This explanation would be consistent with identical dissociation constants for tetramer dissociation and fast phase dissociation from the decamers. For eIF2-binding, the βH160D decamers can therefore be thought of as more like isolated tetramers. That is, eIF2 readily associates but then is likely to dissociate too rapidly for efficient catalysis.

We further interrogated the biphasic dissociation behavior of eIF2 from WT and βH160D decamers by varying the time allowed for eIF2 binding to eIF2B (Figure 3 – figure supplement 1A-B). For both WT and βH160D we observed an exponential decrease in the percentage of fast phase dissociation, which within two minutes plateaued at ~11% fast phase dissociation for eIF2 binding to WT and at ~55% fast phase dissociation for eIF2 binding to βH160D decamers (Figure 3G). These data argue that at equilibrium the fast phase dissociation plays a small part in the engagement between eIF2 and WT eIF2B but plays a significant part in substrate engagement with βH160D decamers. This kinetic behavior can be explained by a model proposing stepwise engagement between eIF2 and eIF2B in a process that first entails engagement of 3 interaction interfaces (IF1-3), followed by a second, slower step that engages the fourth interaction interface (IF4; Figure 3H-I). In this model, the βH160D mutation does not affect the on/off rates of eIF2 engagement with eIF2B through interfaces 1-3, but slows the on-rate (k_2 in Figure 3H-I) of converting from 3 interface engagement to 4 interface engagement. Such a mechanism can explain the accumulation of the "intermediate" fast phase dissociation species.

We next assessed eIF2-P binding to the immobilized eIF2B species. For both WT and βH160D decamer binding, this interaction could be modeled using one-phase association and dissociation kinetics. The overall affinity of eIF2-P for both species was largely comparable (WT K_D = 14 nM; βH160D K_D = 8.1 nM) (Figure 3D-E). As expected owing to the absence of the dimeric eIF2Bα subunit, which constitutes part of the eIF2-P binding site, we observed no noticeable eIF2-P binding to WT tetramers (Figure 3F).

234 From these results, we conclude that the βH160D decamer shares a number of
235 properties with the eIF2-P-bound decamer: 1) reduced intrinsic GEF activity, 2) impaired
236 substrate binding, and 3) insensitivity to ISRIB. Owing to these similarities, we wondered
237 whether the βH160D mutation mimics eIF2-P binding and shifts eIF2B into an I-State or
238 'I-State like' conformation. To assess this notion, we determined the structure of the
239 βH160D eIF2B decamer using single-particle cryo-EM.
240
241 **The βH160D mutation shifts eIF2B into an inhibited conformation**
242 We prepared the βH160D decamer by combining βH160D tetramers and eIF2Bα_2, and
243 subjected the sample to cryo-EM imaging. After 2D and 3D classification, we generated
244 a single consensus structure of the βH160D decamer at 2.8 Å resolution (Table 2, Figure
245 4 - figure supplement 1) with most side chains clearly resolved (Figure 4A, Figure 4 –
246 figure supplement 1E-F). This map allowed us to build an atomic model of how the
247 βH160D substitution alters the conformation of the eIF2B decamer. By superimposing
248 the βH160D decamer structure and our previously published A-State structure (eIF2B-
249 eIF2 complex, PDB ID: 6O81), we observed a significant difference in their overall
250 architecture: the two tetramer halves of the βH160D decamer underwent a rocking
251 motion that changed the angle between them by approximately 3.5° (Figure 4B). This
252 rocking motion repositions the two tetramer halves in an orientation comparable to the I-
253 State structure (eIF2B-eIF2αP complex, PDB ID: 6O9Z), although not reaching the 6°
254 angle observed for the eIF2-P-inhibited decamer (Figure 4 – figure supplement 2). To
255 further understand how the βH160D mutation affects the conformation and dynamics of
256 the decamer, we performed additional cryo-EM analysis of both the WT and the βH160D
257 decamer particles (Figure 4 – figure supplement 3-5). We found the following: 1) in both
258 the WT and the mutant, the two tetrameric halves can undergo rocking motions around
259 the central axis; 2) the βH160D mutation shifts the mean conformation of the decamer
260 towards the I-State; and 3) the βH160D dataset likely represents particles that follow a
261 continuous conformation distribution, rather than a mixture of distinct A and I-State
262 populations. These observations validate our hypothesis that the βH160D mutation shifts
263 eIF2B from the active conformation towards an inhibited conformation.
264
265 We next examined changes to the ISRIB-binding pocket. Comparing the βH160D
266 decamer to A-State (eIF2-bound eIF2B) and I-State (eIF2α-P-bound eIF2B) structures,
267 we noticed that its ISRIB binding pocket was 3.3 Å wider in its long dimension than that

268 of the A-State (Figure 5A), again reminiscent of the I-State (Figure 5C). The widening of
269 the binding pocket can explain why ISRIB fails to assemble βH160D tetramers into
270 octamers or affect GEF activity.
271
272 Zooming in on the tetramer-tetramer interface, we examined the interactions in the WT
273 eIF2B A-State decamer that stabilize the dimerization interface (Figure 5B). In the WT
274 decamer, βH160 forms a π-π stacking interaction with δ'F452, which is lost in the
275 βH160D eIF2B decamer and leads to the retraction of the short loop bearing this residue
276 (Figure 5B and Figure 5 – figure supplement 1). Other interactions in WT decamer
277 include an ionic interaction between β'R228 and δ'D450, as well as a cation-π interaction
278 between β'R228 and δ'F452. In the βH160D decamer, β'R228 repositions itself within the
279 network of three negative charges (βE163, βD160 and δ'D450) and one aromatic amino
280 acid (δ'F452) to reach a new stable state locally. The loop movement caused by the
281 mutation propagates across the entire tetramer, resulting in the rocking motion observed
282 in Figure 4B. This explains how the βH160D amino acid change in eIF2B remodels the
283 dimerization interface to widen the ISRIB binding pocket and induce an I-State like
284 conformation.
285
286 To further examine the long-range effect of this interface mutation, we looked at the
287 critical interfaces for substrate (eIF2) binding provided by eIF2Bβ and eIF2Bδ. An
288 overlay of the βH160D decamer structure with the eIF2B-eIF2 complex structure
289 revealed that the substrate eIF2α binding pocket was widened by 2.9 Å (Figure 5F). As
290 established before (Schoof et al. 2021), a similar pocket widening is observed in the I-
291 State structure of eIF2B (2.6 Å induced by eIF2α-P binding). This widening is predicted
292 to prevent eIF2 from properly engaging the fourth binding site on eIF2Bδ' and hence
293 turns the decameric eIF2B into conjoined tetramers such that only three of the four eIF2-
294 eIF2B binding interfaces remain readily accessible to eIF2 binding. Our structural
295 observations, therefore, explain the decrease in eIF2 binding and reduction in GEF
296 activity of the βH160D decamer. The remaining portion of slow phase dissociation of
297 eIF2 from βH160D decamers, though, indicates that engagement with all 4 interfaces,
298 while disfavored, is not impossible as is the case with the pure tetrameric species). By
299 contrast, the inhibitor (eIF2α-P) binding site (Figure 5G) was not changed significantly
300 compared to the eIF2B-eIF2α-P complex structure. This observation is consistent with
301 the similar binding affinities measured for eIF2-P towards the βH160D decamer and the

302 WT decamer. We conclude that the βH160D mutation shifts the eIF2B decamer into a
303 conformation closely resembling the I-State.
304
305 **eIF2B βH160D mutation leads to stress-independent ISR activation**
306 Given that the eIF2B βH160D mutation biases eIF2B's conformation towards an I-State
307 like conformation, reducing its GEF activity, we predicted that expression of eIF2B
308 βH160D in cells would lead to constitutive ISR activation. To test this notion, we
309 introduced the βH160D mutation into the genome of HEK293FTR cells by editing the
310 endogenous eIF2Bβ gene (*EIF2B2*) (Figure 6 – figure supplement 1A). Using
311 CRISPR/Cas9 technology, we obtained two such lines. One cell line yielded a
312 homozygous clone in which all alleles were edited (line βH160D #1) (Figure 6 – figure
313 supplement 1B-C). The other was a heterozygous clone containing one edited allele
314 while the remaining alleles were knocked out through CRISPR/Cas9-induced frameshift
315 mutations (line βH160D #2). Critically, both βH160D cell lines showed eIF2Bβ and
316 eIF2Bε protein levels comparable to the unedited parental cells, demonstrating that the
317 mutation does not destabilize eIF2Bβ or other complex members and that compensatory
318 mechanisms must normalize the gene dosage imbalance in clone #2 (Figure 6A)
319 (Wortham et al. 2016). We observed constitutive, low-level activation of the ISR in both
320 clones, exemplified by elevated levels of ATF4 protein in the absence of stress (Figure
321 6A, lanes 5 and 9 vs lane 1). ATF4 induction was still responsive to induced stress with
322 thapsigargin (lanes 7 and 11) but could not be alleviated by ISRIB treatment in the
323 βH160D lines, both in the absence or presence of stressor (Figure 6A). ATF4 is
324 translationally upregulated during the ISR and, accordingly, ATF4 mRNA levels
325 remained unchanged between WT and the two βH160D clones (Figure 6B). However, as
326 expected, key ATF4 transcriptional targets (such as *DDIT3, ASNS, and CARS*) were
327 upregulated in βH160D cells, confirming that increased ATF4 mRNA translation leads to
328 production of active ATF4, which in turn activates transcription of its downstream stress-
329 responsive genes (Figure 6B).
330
331 The second hallmark of an active ISR is the general inhibition of translation initiation
332 and, hence, a reduction in protein synthesis. To monitor protein synthesis, we treated
333 WT and βH160D cells with puromycin and assessed puromycin incorporation in nascent
334 polypeptide chains by immunoblotting. Both βH160D cell lines displayed significantly
335 reduced levels of basal protein synthesis (βH160D #1 cells: 47 ± 9.0%; βH160D #2 cells:

336 69% ± 7.3%, both compared to WT), again consistent with constitutive activation of the
337 ISR (Figure 6C, Figure 6 – figure supplement 2). WT and βH160D cells did not differ in
338 eIF2α phosphorylation levels, underlining the observation that the impairment of eIF2B
339 GEF activity caused by this mutation is sufficient to induce a constitutive ISR (Figure 6C,
340 Figure 6 – figure supplement 3A-B).
341
342 Phenotypically, the constitutive ISR activation was accompanied by slow cell growth: cell
343 doubling time increased from 25.7 ± 3.6 h for WT cells to 38.4 ± 3.5 h for βH160D (#1)
344 cells and could not be rescued by ISRIB treatment (Figure 6D, Figure 6 – figure
345 supplement 3C) .

346 **Discussion**

347 Here, we show that a single engineered H to D mutation in eIF2Bβ alters the
348 conformation of the eIF2B decamer, resulting in altered dissociation kinetics of substrate
349 eIF2, a ~three-fold reduction of intrinsic enzymatic activity, and resistance to ISRIB
350 rescue. In cells, this hypomorphic mutation culminates in a constitutively activated low-
351 level ISR. The structural, biochemical, and cellular changes resulting from the βH160D
352 mutation are evocative of the Inhibitor (eIF2-P) bound state of eIF2B ('I-State'). In
353 conjunction with our prior assessment of changes in eIF2B induced by eIF2α-P binding,
354 these orthogonal data underscore how the conformational changes brought about by
355 eIF2α-P binding govern ISR activation (A/I-State model) and that even the presence of
356 eIF2α-P is dispensable as long as an I-State or I-State like conformation is maintained.
357

358 eIF2B is a far more dynamic complex than we realized just a year ago. Small molecules
359 (ISRIB and its derivatives), the natural substrate (eIF2), and viral proteins (SFSV NSs)
360 can stabilize eIF2B in its active A-State (Kashiwagi et al. 2021; Schoof, Wang, et al.
361 2021; Schoof et al. 2021; Zyryanova et al. 2021). Conversely, binding of the inhibitor
362 (eIF2-P) can compete with these molecules by shifting the decamer to the inhibited I-
363 State (Schoof et al. 2021; Zyryanova et al. 2021). Although the conformational
364 displacements induced by βH160D are in many aspects similar to those of the eIF2-P
365 bound I-State when compared to the A-State, they are not identical. While the cryo-EM
366 data show a comparable widening of the eIF2α binding pocket, the movement of the β-
367 solenoid in eIF2Bε is less pronounced in βH160D decamers than in the eIF2-P bound I-
368 State (Figure 4 – figure supplement 2), likely because the rocking motion induced by
369 βH160D originates near the ISRIB pocket, not from the eIF2-P binding site. In addition,
370 despite extensive classification calculations, we did not recover single-particle images of
371 the βH160D complex belonging to the A-State, arguing against the idea that the βH160D
372 structure is a mixture of A-State and I-State structures. The βH160D decamer rather
373 represents a continuous distribution of conformations with a more restricted range of
374 motion compared to the WT decamer, and for which the average converges to an I-State
375 like model. Hence, acknowledging both similarities and differences to the I-State, we
376 refer to the conformation induced by βH160D as 'I-State like'.
377

378 The conformational changes brought about by eIF2-P binding result in a specific
379 enzymatic activity (quantified in the specificity constant k_{cat}/K_M) that is approximately 2

380 orders of magnitude reduced from that of the A-State (Schoof et al. 2021). By
381 comparison, the βH160D mutation causes the specificity constant to drop by only ~2 fold
382 (Figure 2). Nevertheless, despite the comparatively small change in eIF2B activity, the
383 mutation induces constitutive ISR activation, suggesting that cells are sensitive to small
384 fluctuations in eIF2B GEF activity. These numbers also tell us that there is still potential
385 for more robust ISR activation. Indeed, treating βH160D cells with relatively low amounts
386 (10 nM) of an eIF2-P inducing stressor like thapsigargin further enhances ATF4
387 translation (Figure 6A). The latter result also suggests that the mutation is compatible
388 with even more potent inhibition mediated by eIF2-P binding. This conclusion is further
389 supported by our 3D reconstructions and the SPR studies, which show that the βH160D
390 mutation does not appreciably affect eIF2-P binding.
391
392 We demonstrate that both intrinsic enzymatic activity and substrate (eIF2) binding are
393 affected in the I-State like βH160D decamer. It remains unclear how the conformational
394 changes in either this structure or that in the eIF2-P bound I-State (Schoof et al. 2021)
395 engender a reduced k_{cat}, especially given that βH160 is located far from the catalytic
396 center. Non-ideal positioning of substrate molecules that still engage an I-State or I-State
397 like decamer may explain the reduced rate of nucleotide exchange. Further speculation
398 regarding the mechanism is limited by a lack of structural data for certain critical regions.
399 The eIF2Bε catalytic domain is absent from all but the substrate (eIF2) bound structures.
400 The eIF2Bε linker, a known regulatory region connecting the catalytic domain to the core
401 of eIF2Bε, is similarly unresolved, as are the poorly understood C-terminal solenoid "ear
402 domains" of eIF2Bγ (Welsh and Proud 1993). The conformation and positioning of these
403 and other regions may be affected during the ISR and play roles in regulation of eIF2B's
404 activity that warrant further examination. With the recent discovery that eIF2B can
405 directly read out and respond to sugar phosphate levels, there may be a host of
406 functions and mechanisms of regulation for eIF2B still to be uncovered (Hao et al. 2021).
407
408 Our SPR data (Figure 3) demonstrate that the effects of the βH160D mutation on
409 substrate (eIF2) binding result from changes to the relative proportion of rapidly
410 dissociating eIF2 molecules. Substrate association, however, remains unaffected. The
411 biphasic dissociation behavior, usually observed for multivalent ligands due to avidity
412 effects, is not entirely unexpected. Substrate-bound structures of eIF2B decamer
413 previously revealed four binding interfaces (IF1-IF4) between eIF2 and eIF2B. Hence, it

414 is possible that stochastic partial binding occurs for a fraction of substrate molecules
415 when the IF4 interface is too distant from IF3 for both to be engaged by eIF2. eIF2α-P
416 binding (or the βH160D mutation) pulls IF4 away from IF3, increasing the probability of
417 this partially engaged binding mode, thus reducing the substrate binding affinity. Notably,
418 though, the biphasic dissociation is not observed for inhibitor (eIF2-P) binding, where
419 both association and dissociation can be fit to monophasic models. This observation
420 suggests greater conformational flexibility along the combinatorial eIF2 binding surfaces
421 than along the eIF2-P binding surfaces.
422
423 The βH160 residue is highly conserved amongst eukaryotes. To date, no variation has
424 been reported at this position in the human genome. However, the mechanism by which
425 the βH160D mutation impacts eIF2B activity raises the possibility that certain VWMD
426 mutations may likewise compromise eIF2B function through alteration of conformational
427 state. The disease-associated βE213G mutation (ClinVar VCV000004336), for example,
428 localized near the ISRIB pocket and far away from the catalytic center, reportedly does
429 not affect complex association but substantially reduces GEF activity (Li et al. 2004).
430 Understanding the precise mechanism of eIF2B inactivation in individual VWMD patients
431 may be critical for patient stratification and proper treatment. Although ISRIB is unable to
432 rescue the βH160D defect, it is plausible that other analogs (or molecules acting at a
433 different site) with higher affinities than ISRIB may be able to overcome the charge
434 repulsion and restore the A-State conformation, demonstrating the importance of
435 continued endeavors to uncover molecules and strategies to inhibit or activate the ISR
436 orthogonally.

437 **Figures**

438

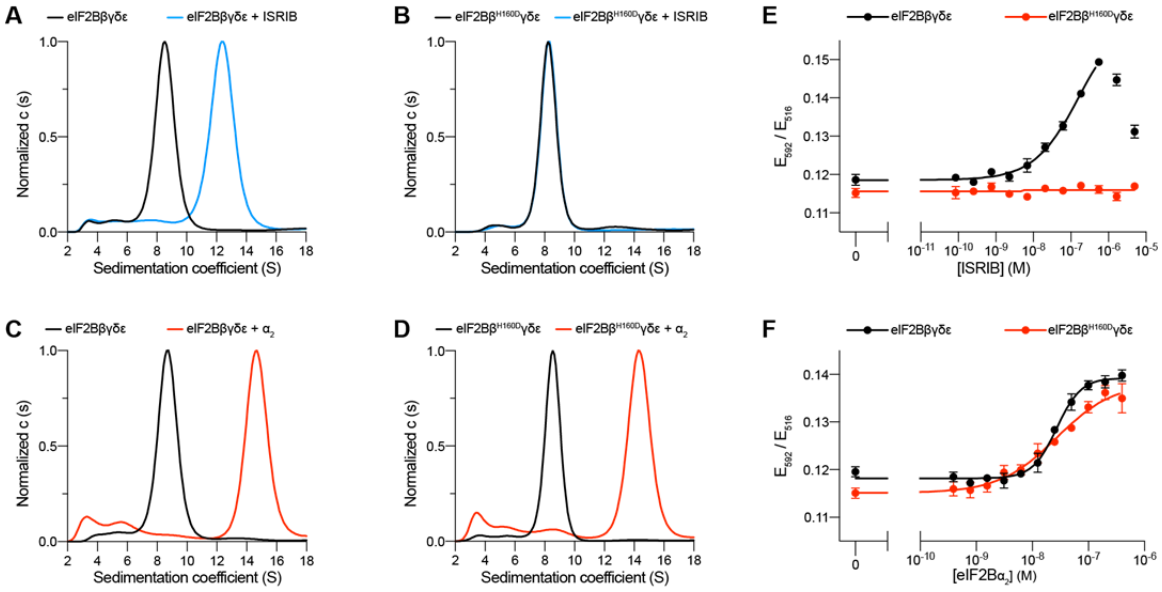

439

440

441 **Figure 1. The eIF2B βH160D mutation prevents octamer assembly but not decamer**

442 **assembly.**

443 **(A-D)** Characterization by analytical ultracentrifugation (sedimentation velocity) of (A)

444 500 nM eIF2Bβδγε +/- 1 μM ISRIB, (B) 500 nM eIF2Bβ^{H160D}δγε +/- 1 μM ISRIB, (C) 500

445 nM eIF2Bβδγε +/- 500 nM eIF2Bα$_2$, and (D) 500 nM eIF2Bβ^{H160D}δγε +/- 500 nM eIF2Bα$_2$.

446 The eIF2Bβδγε tetramer sediments with a sedimentation coefficient of ~8 S, the

447 eIF2B(βδγε)$_2$ octamer at ~12 S, and the eIF2B(αβδγε)$_2$ decamer at ~14 S. **(E-F)** FRET

448 signal (E_{592}/E_{516}) measured after 1 h of eIF2Bβδγε-F tetramers incubation with (E) ISRIB

449 or (F) eIF2Bα$_2$. For assembly by ISRIB, WT EC_{50} = 170 ± 25 nM. For assembly by

450 eIF2Bα$_2$, WT EC_{50} = 29 ± 3 nM and βH160D EC_{50} = 33 ± 3 nM. WT and βH160D

451 eIF2Bβδγε-F tetramers at 50 nM throughout. For (E-F), representative replicate

452 averaging four technical replicates are shown. Biological replicates: n = 3. All error bars

453 and '±' designations are s.e.m.

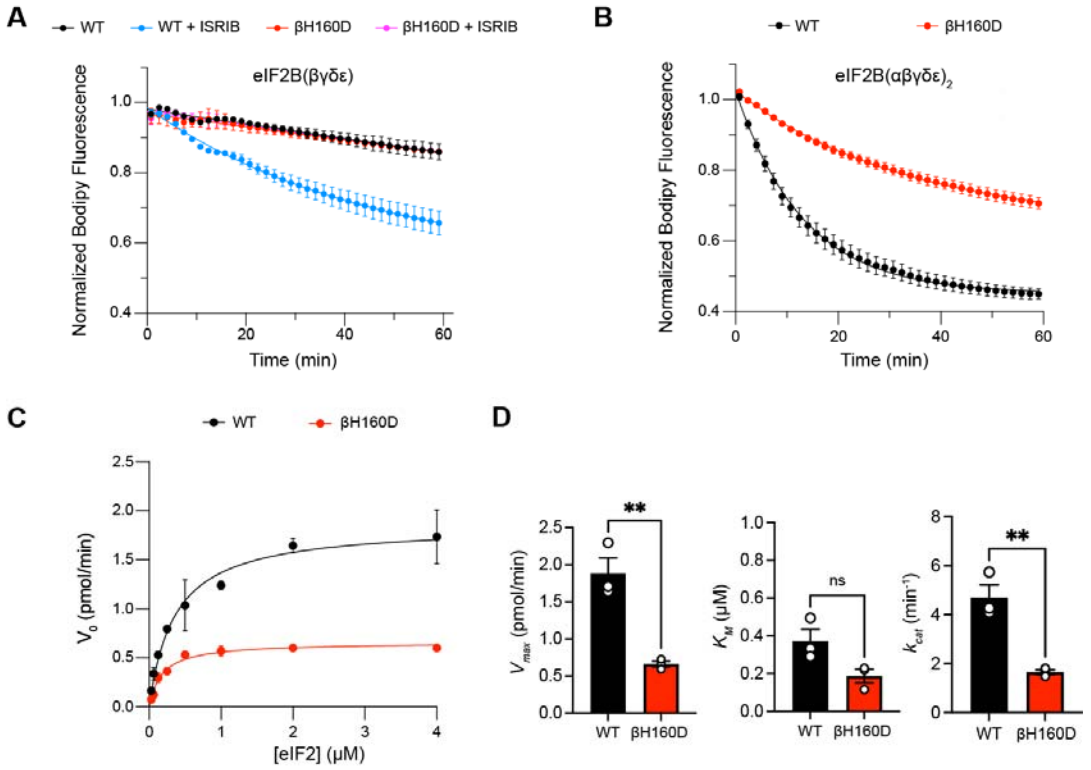

Figure 2. **The βH160D mutation impairs nucleotide exchange by the eIF2B holoenzyme.**

(**A-B**) GEF activity of eIF2B as assessed by BODIPY-FL-GDP exchange on eIF2 using (A) eIF2B tetramer (100 nM) and (B) eIF2B decamer (10 nM). For (A), ISRIB only stimulates eIF2B guanine nucleotide exchange (GEF) activity for the WT tetramer ($t_{1/2}$ = 31.1 ±1.47 min). In (B), the βH160D decamer has lower GEF activity ($t_{1/2}$ = 23.57 ± 0.82 min) than WT decamer ($t_{1/2}$ = 9.28 ± 0.96 min)). (**C**) Michaelis-Menten fit of the initial velocity of eIF2B-catalyzed nucleotide exchange as a function of eIF2 concentration (10 nM eIF2B decamer throughout). **(D)** Kinetic parameters of the Michaelis-Menten fit. βH160D decamers have ~3-fold reduced intrinsic enzymatic activity (WT V_{max} = 1.86 ± 0.13 pmol/min; βH160D V_{max} = 0.66 ± 0.03 pmol/min; two-sided t-test p = 0.0045) and turnover number (WT k_{cat} = 4.70 ± 0.52 min^{-1}; βH160D k_{cat} = 1.65 ± 0.10 min^{-1}; two-sided t-test p = 0.0045). The K_M is not significantly different (WT K_M = 0.36 μM ± 0.09 μM; βH160D K_M = 0.18 ± 0.03 μM; two-sided t-test p = 0.07). Biological replicates: n = 2 for (A), and n = 3 for (B-D). All error bars and '±' designations are s.e.m.

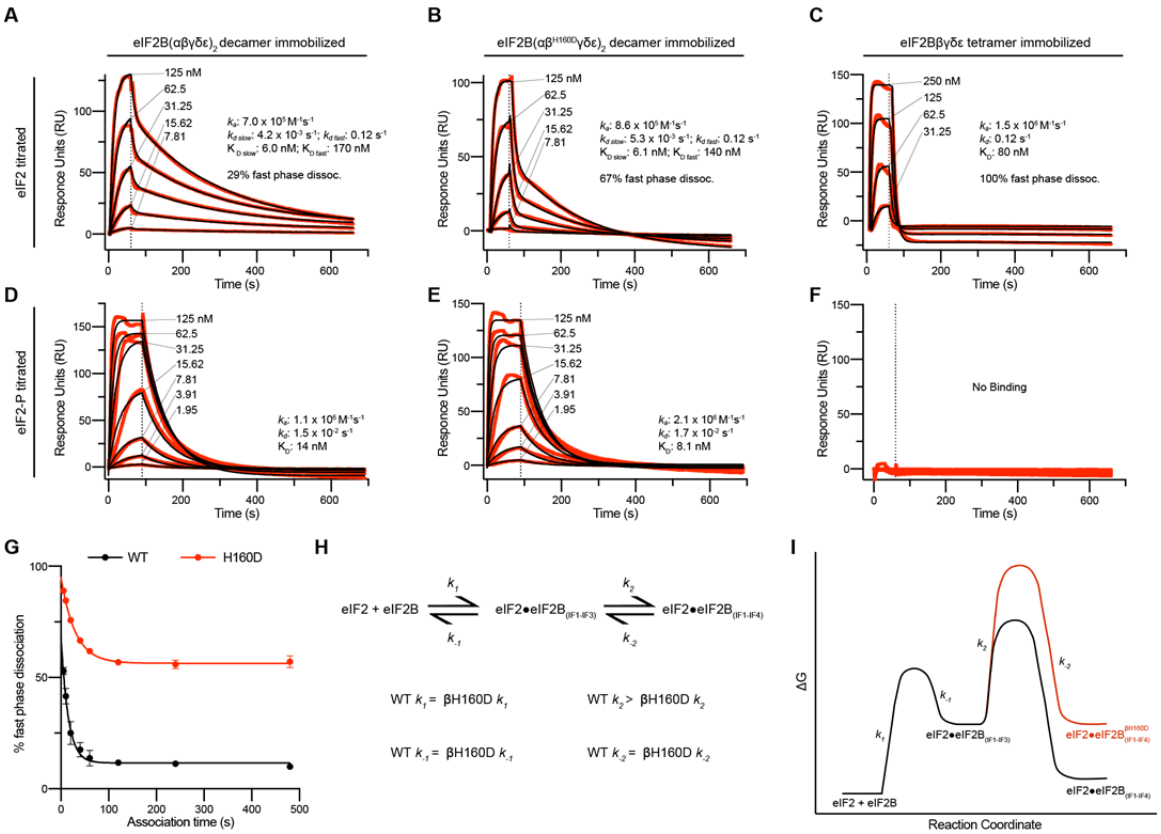

Figure 3. **Substrate (eIF2) binding to eIF2B is compromised by the βH160D mutation.**

(**A-F**) SPR of immobilized (A and D) WT eIF2B decamer, (B and E) βH160D eIF2B decamer, and (C and F) WT eIF2B tetramer binding to 2-fold titrations of (A-C) eIF2 or (D-F) eIF2-P. For WT eIF2B decamer and βH160D eIF2B decamer, eIF2Bα was Avi-tagged and biotinylated. For WT eIF2B tetramer, eIF2Bβ was Avi-tagged and biotinylated. Binding was modeled as one-phase association for (A-E), two-phase dissociation for (A-B), and one-phase dissociation for (C-E). **(G)** SPR of immobilized WT eIF2B decamer and βH160D eIF2B decamer was performed with eIF2 at 62.5 nM throughout and varied association time from 5-480 s. The dissociation kinetics were then modeled (individual traces shown in Figure 3 – figure supplement 1) and from this data percent fast phase dissociation was plotted as a function of association time with a single exponential fit. WT $t_{1/2}$ = 10.4 s; βH160D $t_{1/2}$ = 20.7 s. Percent fast phase dissociation is always higher for βH160D decamers vs. WT decamers and reaches an equilibrium at ~55% fast phase dissociation for βH160D decamers and ~11% fast phase dissociation for WT decamers. **(H)** Model reaction scheme of eIF2 engagement with eIF2B. k_1, k_{-1}, and k_{-2} each are comparable for WT and βH160D decamers but WT k_2 >

βH160D k_2. Based on the SPR data in Figure 3 A-C, k_1 ~ 7.0 x 10^5 $M^{-1}s^{-1}$ and k_{-1} ~ 0.12 s^{-1}. k_{-2} is calculated under the assumption that slow phase dissociation represents the combination of k_{-1} and k_{-2} dissociation. k_{-1} is fast phase dissociation, so $k_{-1} = k_{d\ fast}$. Hence from $k_{-1} * k_{-2} = k_{d\ slow}$ we get that 0.12 s^{-1} * k_{-2} = 5.3 x 10^{-3} s^{-1}. Therefore k_{-2} ~ 0.044 s^{-1}**. (I)** Free energy profile of eIF2 engagement with eIF2B either in the WT (black) or βH160D (black then red) context. Initial 3 interface engagement is energetically the same for either WT or βH160D, but engagement with the 4th interface is disfavored in the βH160D mutant. The free energy profile is drawn at sub saturating conditions. Given the percent fast phase vs slow phase dissociation at equilibrium in Figure 1G we know that for WT, [eIF2•eIF2B$_{(IF1-IF4)}$] / [eIF2•eIF2B$_{(IF1-IF3)}$] ~8 while for βH160D [eIF2•eIF2B$_{(IF1-IF4)}$] / [eIF2•eIF2B$_{(IF1-IF3)}$] ~1. For (G), n = 3 biological replicates. All error bars and '±' designations are s.e.m.

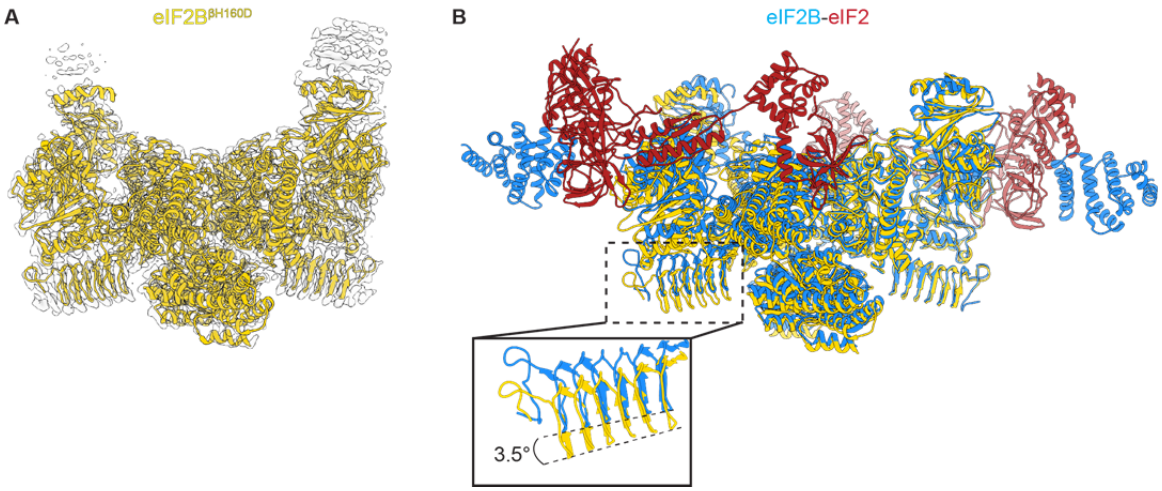

Figure 4. **Overall architecture of eIF2B$^{\beta H160D}$.**

(A) Atomic model of eIF2B$^{\beta H160D}$ decamer (yellow) superimposed into the cryo-EM map (grey), showing the overall structure of the molecule. **(B)** Overlay of the eIF2B$^{\beta H160D}$ structure to the eIF2B-eIF2 structure (PDB ID: 6O81) shows a 3.5° hinge movement between the two eIF2B halves. eIF2B$^{\beta H160D}$ is shown in gold; eIF2B in the eIF2B-eIF2 structure in blue; eIF2 in red.

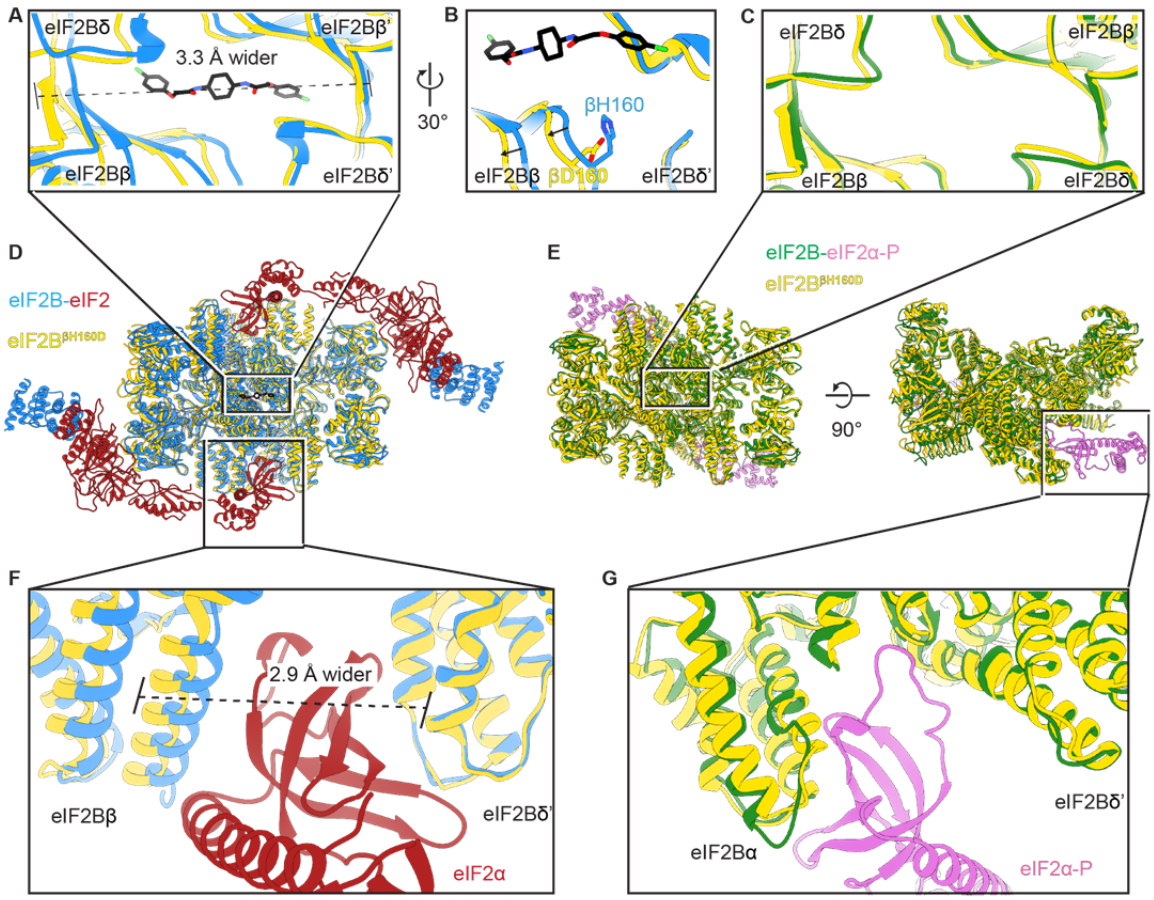

Figure 5. The βH160D mutation conformationally diminishes eIF2B activity. **(A)** Overlay of the eIF2B$^{\beta H160D}$ structure to the eIF2B-eIF2 structure showing a ~ 3 Å lengthening of the ISRIB-binding pocket in the eIF2B$^{\beta H160D}$ structure. The pocket lengthening is measured between eIF2Bδ and eIF2Bδ' L482; the 'prime' indicates the subunit of the opposing tetramer. ISRIB is shown in stick representation. **(B)** A rotated view of panel (A) showing that in the eIF2B$^{\beta H160D}$ structure the loop bearing βD160 retracts from the opposite tetramer due loss of some attractive interactions (for details, see Figure 5 – figure supplement 1). **(C)** Overlay of the eIF2B$^{\beta H160D}$ structure to the eIF2B-eIF2α-P structure showing the similar dimensions of the ISRIB binding pockets. **(D)** Zoom out of the overlay in panels (A), (B), and (F). **(E)** Zoom out of the overlay in panel (C) and (G). **(F)** Overlay of the eIF2-bound eIF2B to eIF2B$^{\beta H160D}$ showing the 2.9 Å widening of the eIF2α binding pocket induced by the βH160D mutation. The pocket widening is measured between eIF2Bβ E139 and eIF2Bδ' R250. **(G)** Overlay of the eIF2α-P-bound eIF2B to eIF2B$^{\beta H160D}$ showing the similar dimensions of the eIF2α-P binding pockets. Protein molecules are colored as in Figure 4. ISRIB is colored in CPK.

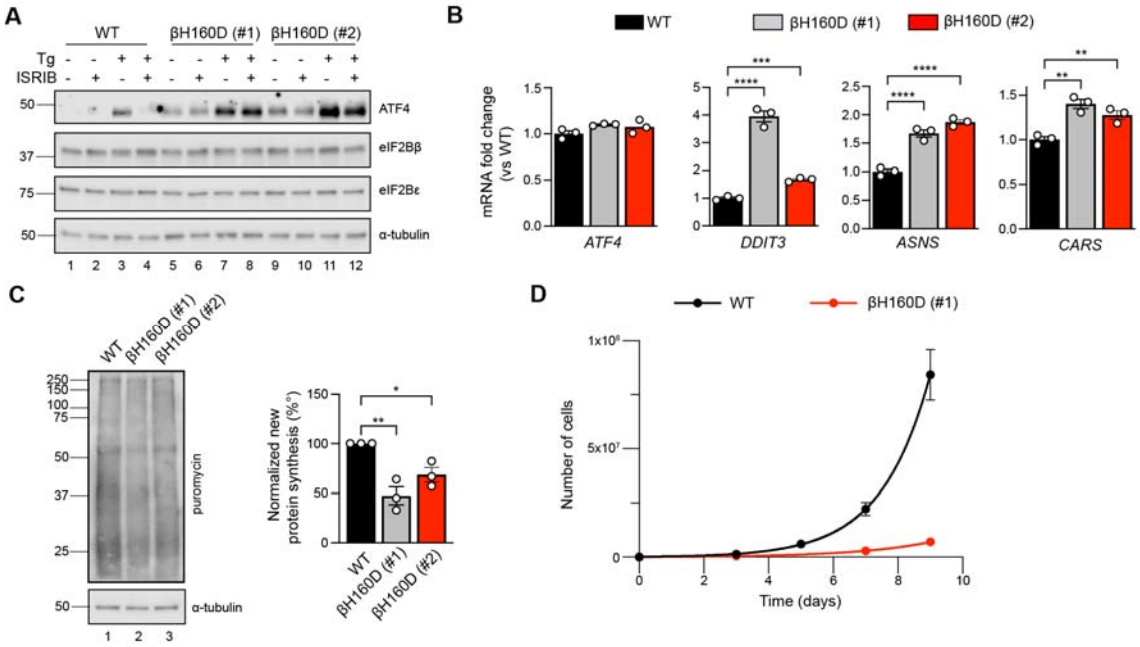

Figure 6. **The βH160D mutation spontaneously activates the ISR in cells.** (**A**) Western blot of WT vs *EIF2B2*^{H160D} HEK293FTR cell lines (βH160D (#1) and βH160D (#2)) treated with and without stress (10 nM thapsigargin (Tg)) or ISRIB (200 nM) for 1 h. eIF2B subunit levels do not differ between cell lines. ATF4 is constitutively produced in the βH160D cell lines (lanes 5 and 9, compare to lane 1), and its induction is ISRIB-insensitive (lanes 6, 8, 10, 12, compare with lane 4). α-tubulin serves as a loading control. (**B**) RT-qPCR for *ATF4* and *ATF4* transcriptional targets in untreated WT vs. βH160D cell lines. Transcript levels were normalized to *GAPDH* signal and fold changes were calculated with WT level set to 1. While there is no difference in *ATF4* transcript level, the *ATF4* target genes *DDIT3* (CHOP), *ASNS,* and *CARS* are significantly transcriptionally upregulated in the βH160D lines (one-way ANOVA with Dunnett post-hoc tests). (**C**) Puromycin incorporation assay for new protein synthesis. Left panel: representative blot of cell lysates treated with a 10 min puromycin pulse and blotted for puromycin (new protein synthesis) or tubulin (loading control). Right panel: quantification of puromycin incorporation. The puromycin signal is normalized to tubulin levels and set at 100% for WT. Both βH160D cells show a reduction of basal protein translation (one-way ANOVA with Dunnett post-hoc test, p = 0.0026 for WT vs βH160D (#1) and p = 0.0288 for WT vs βH160D (#2)). (**D**) Growth curves showing that βH160D cells grow slower than WT cells (WT doubling time = 25.7 h, s.e.m. = 3.6 h; βH160D doubling time = 38.4 h, s.e.m. = 3.5 h.

546 All error bars and '±' designations are s.e.m. For (B, D) n = 3 biological replicates. For
547 (C), n = 3 biological replicates, each of which was the average of 3 technical replicate
548 transfers.* $p<0.05$, **$p<0.01$, ***$p<0.001$, ****$p<0.0001$.

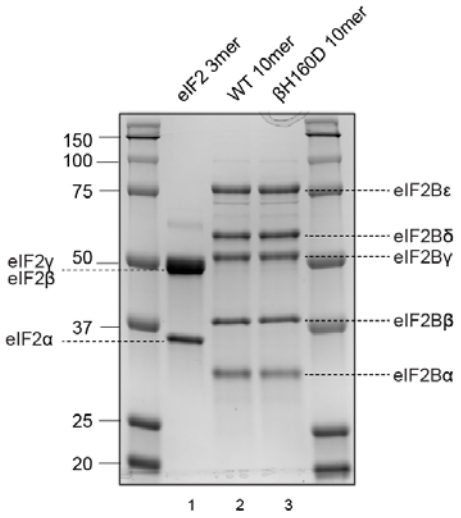

Figure 1 – figure supplement 1. Coomassie-stained gel of purified proteins used in this study.

Human eIF2 trimer was purified from mammalian cells (HEK293) (lane 1). WT and βH160D eIF2B decamers (lane 2 and 3, resp.) were assembled from their respective tetramer (eIF2Bβδγε) and α-dimer (eIF2Bα_2), both purified from *E. coli*.

556

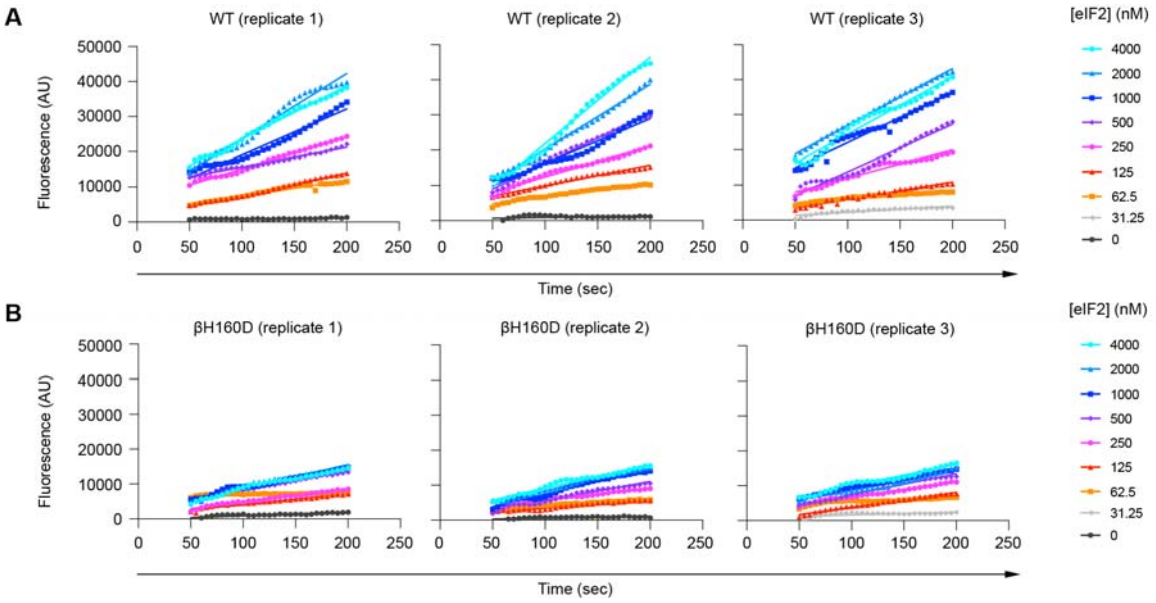

557

558 **Figure 2 – figure supplement 1. The βH160D mutation decreases the initial velocity**
559 **of eIF2B's guanine nucleotide exchange factor (GEF) activity.**
560 BODIPY-FL-GDP loading onto the eIF2 substrate by (A) WT and (B) βH160D eIF2B
561 decamer at varying eIF2 concentrations. Initial velocity was determined by a linear fit to
562 timepoints acquired from 50 to 200 s after addition of eIF2B. Individual replicates are
563 shown. AU = arbitrary units.

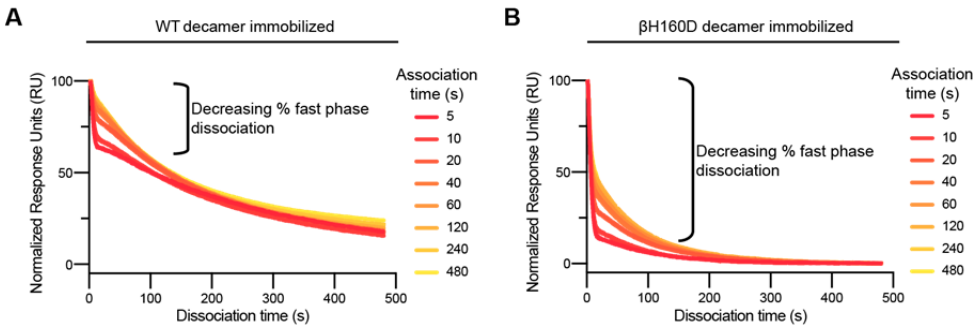

Figure 3 – figure supplement 1. The βH160D mutation increases the fraction of eIF2 molecules that bind and then dissociate with fast phase kinetics.

(**A-B**) Representative dissociation phase SPR traces for eIF2 binding to (A) WT eIF2B decamer or (B) βH160D eIF2B decamer after variable association times ranging from 5 to 480 s. Curves were normalized to maximal signal at the beginning of the dissociation phase. For (A-B), n = 3 biological replicates. All error bars and '±' designations are s.e.m.

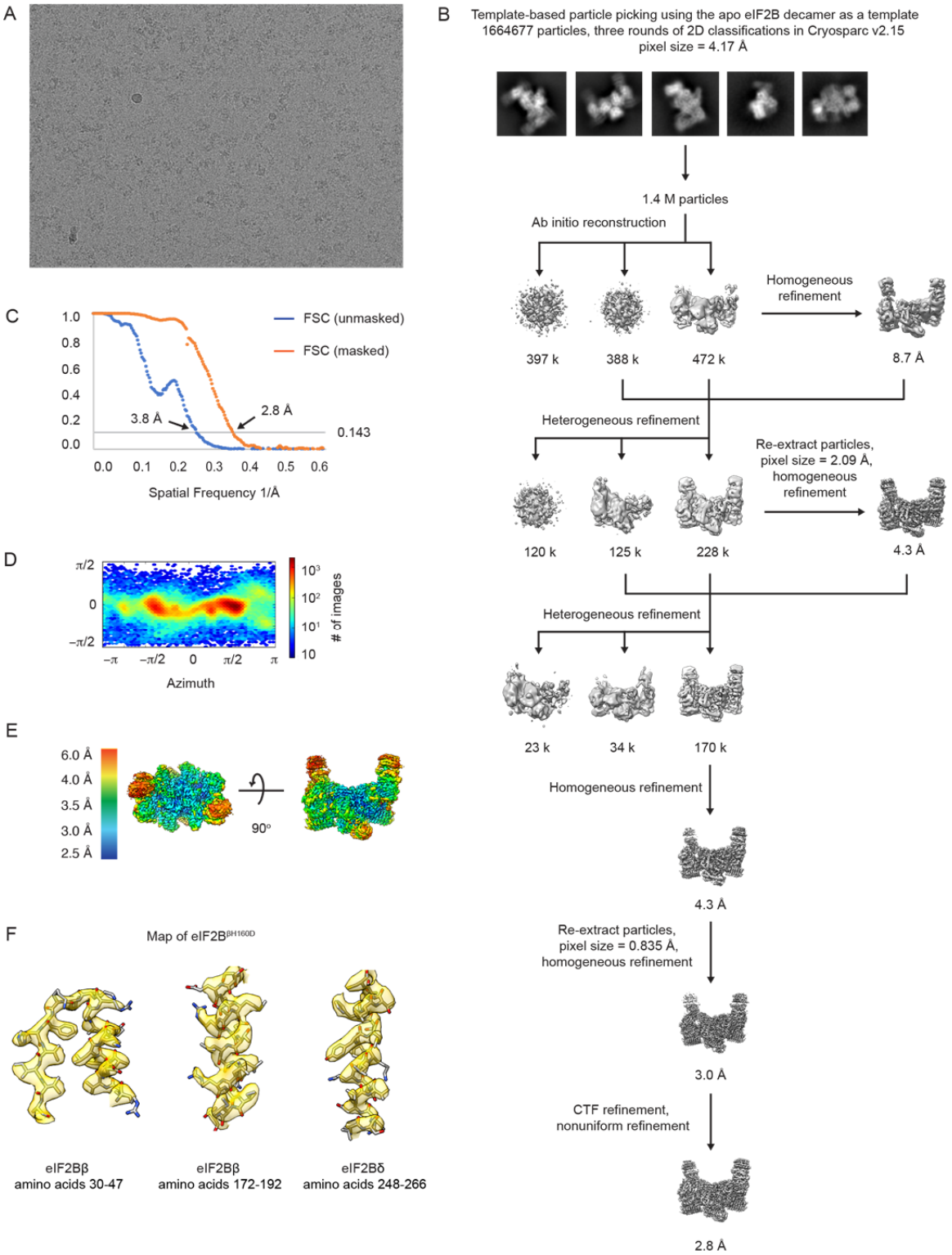

Figure 4 – figure supplement 1. Cryo-EM data analysis of the eIF2B$^{\beta H160D}$ structure. (**A**) Representative micrograph showing the quality of data used for the final reconstruction of the eIF2B$^{\beta H160D}$ structure. (**B**) Data processing scheme of the

576 eIF2B$^{\beta H160D}$ structure. (**C**) Fourier shell correlation (FSC) plots of the 3D reconstructions
577 of eIF2B$^{\beta H160D}$ unmasked (dark blue), masked (orange). (**D**) Orientation angle distribution
578 of the eIF2B$^{\beta H160D}$ reconstruction. (**E**) Local resolution map of the eIF2B$^{\beta H160D}$ structure.
579 (**F**) Electron microscopy maps of different regions of the eIF2B$^{\beta H160D}$ structure showing
580 the quality of the data and the fit of the model.

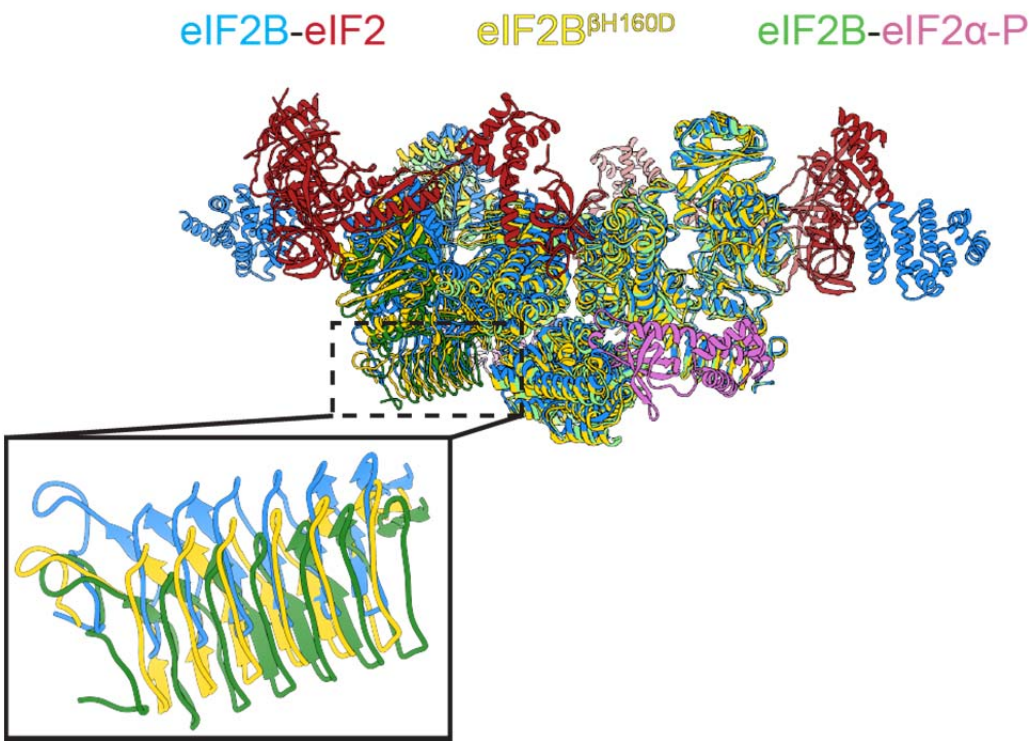

Figure 4 – figure supplement 2. Structure overlay of the A and I state models. Overlay of the A-state model (eIF2-eIF2B complex, PDB ID: 6O81) (blue), the I-State model (eIF2α-P-eIF2B complex, PDB ID: 6O9Z) (green) and the I-State like model (eIF2B$^{\beta H160D}$) (yellow) showing the rocking motion between the two tetrameric halves. The inset shows a zoom-in view of the β-solenoid domain (residues 342 to 466) of eIF2Bε. Compared to the βH160D mutation, eIF2α-P binding causes a greater rocking motion in eIF2B.

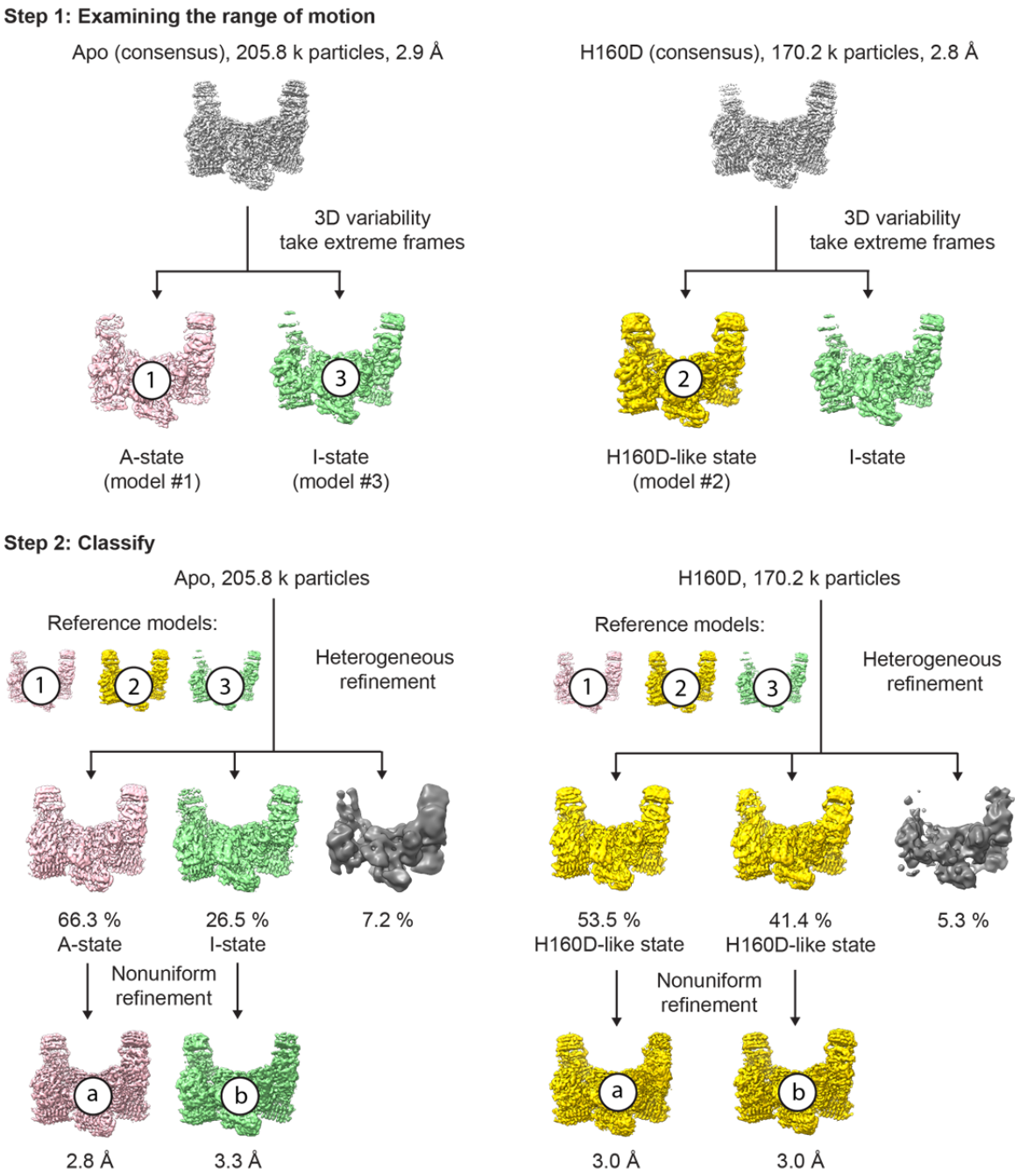

Figure 4 – figure supplement 3. Cryo-EM analysis of the conformation and dynamics of the WT decamer and the βH160D decamer – part 1.

To understand how the βH160D mutation affects the conformation and dynamics of the eIF2B decamer, a multi-step analysis of the cryo-EM data was performed to compare the WT apo eIF2B decamer (abbreviated as “apo”; particles are from the consensus apo eIF2B structure (Schoof et al. 2021)) to the βH160D decamer (abbreviated as “H160D”; particles are from the consensus H160D structure in the current study).

In **step 1**, we performed 3D variability analysis in cryoSPARC for the apo versus the H160D to examine the range of rocking motion between the two tetrameric halves. 20 frames were generated for each structure to represent snapshots of the motion. The first and the last frames represent the two extreme positions of this rocking motion. In the apo structure, the molecule rocks between a state that is very close to the classic A-state (number 1 in the figure) and a classic I-state (number 3 in the figure). In the H160D structure, the molecule rocks between a state that is similar to the consensus H160D state (number 2 in the figure) and a state that is similar to the classic I-state (also similar to the I-state in the apo data). Therefore, H160D and apo both reach similar conformations on the side of the I-state, but apo has a wider range of motion compared to H160D.

Having established the range (by the 3D variability analysis) and the mean position of this motion (the consensus structure) in both apo and H160D, we next determined the particle distribution across these 3 states (1, 2 or 3) in the apo versus the H160D dataset. In **step 2**, we performed heterogeneous refinement of the two datasets separately, using the three models (indicated by numbers 1, 2 and 3 throughout this figure; all maps are low pass filtered to 20 Å) obtained from step 1 as reference models. The apo dataset separated into three classes: 66.3% of all particles went into a class that is similar to the classic A-State (class a), and 26.5 % of all particles went into a class that is similar to the classic I-State (class b), and a small percentage went into a third class that did not result in a high resolution structure. In the H160D dataset, the majority of all particles went into two classes (class a and class b), both of which are similar to the consensus H160D structure.

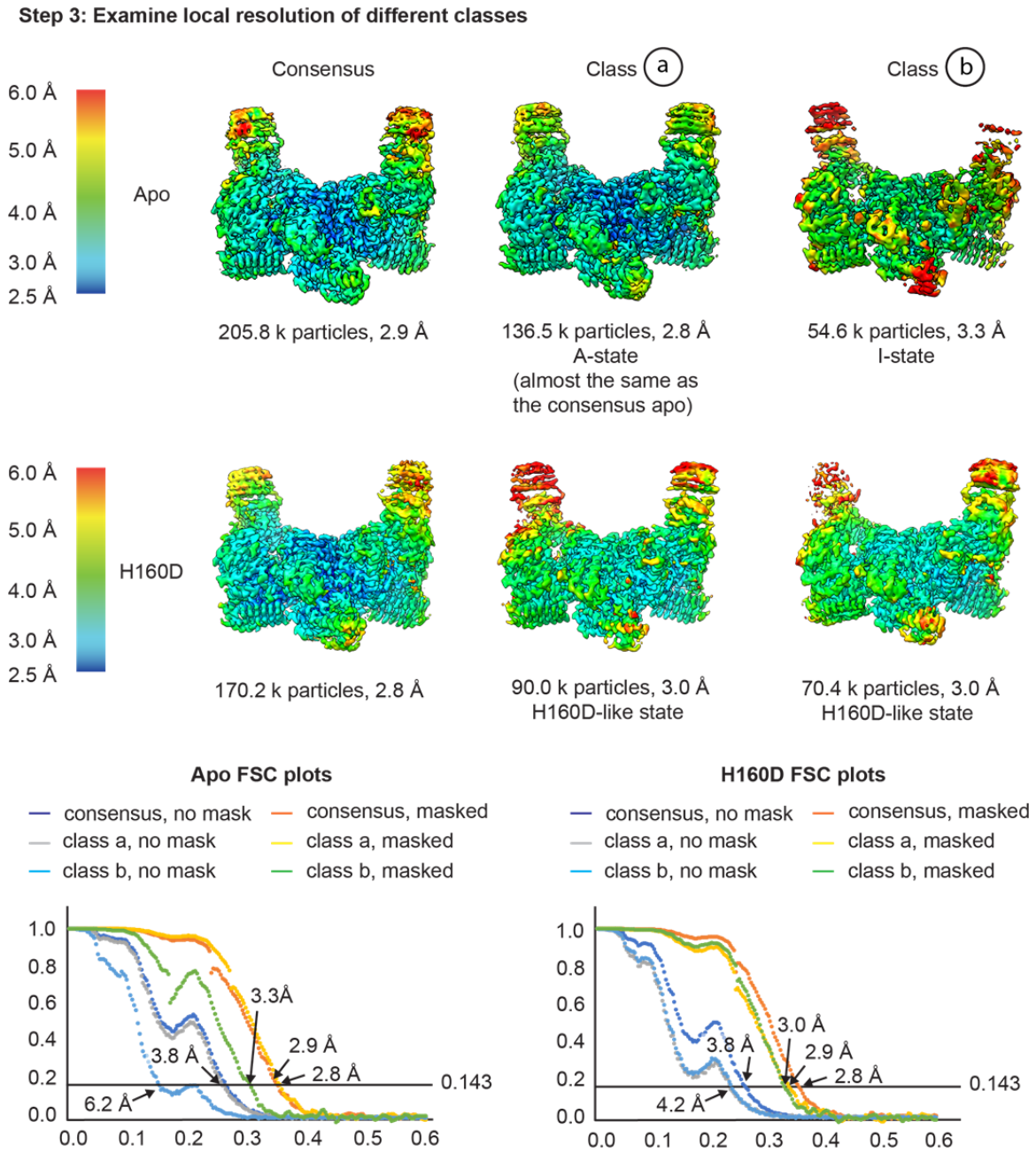

Figure 4 – figure supplement 4. Cryo-EM analysis of the conformation and dynamics of the WT decamer and the βH160D decamer – part 2.

Having finished the 3D classification, we then performed local resolution analysis to examine the quality of the density maps in **step 3** to investigate the potential for different subpopulations of particles within each dataset. As shown in **step 3**, in the apo structure, class a showed a slight improvement in overall resolution (2.8 Å for the class and 2.9 Å for the consensus), as well as improvements in local map quality in the flexible regions of the molecule (see the top of the "wings" in both these maps). Class b has a reduced

633 global resolution, local resolution around the flexible regions, as well as a worse FSC
634 profile (see the FSC plots). Class b could therefore either represent particles that are
635 more I-State like that got separated from the consensus structure, or particles that are
636 more damaged (as suggested by the worse FSC profile and the worse map quality in the
637 flexible regions). For the H160D dataset, classification resulted in two classes that are
638 both similar to the consensus structure (classes a and b) and both classes resulted in
639 worse overall resolution than the consensus (3.0 Å for both classes and 2.8 Å for the
640 consensus). The local resolution of the classes are also worse than the consensus
641 structure in flexible regions. This would suggest that the particles making up the H160D
642 dataset represent a continuous distribution of different conformations, as simply
643 separating them into multiple bins each with fewer particles worsened the map quality of
644 both classes.
645
646 Integrating the results from steps 1 to 3, it is likely that the apo dataset mainly consists of
647 A-State particles, and that the H160D mutation shifts the mean conformation of eIF2B
648 towards a state that is I-like. Also, there is no evidence suggesting that the H160D
649 dataset is a mixture of A- and I-State particles, but rather, particles within this dataset
650 most likely follow a continuous distribution.
651

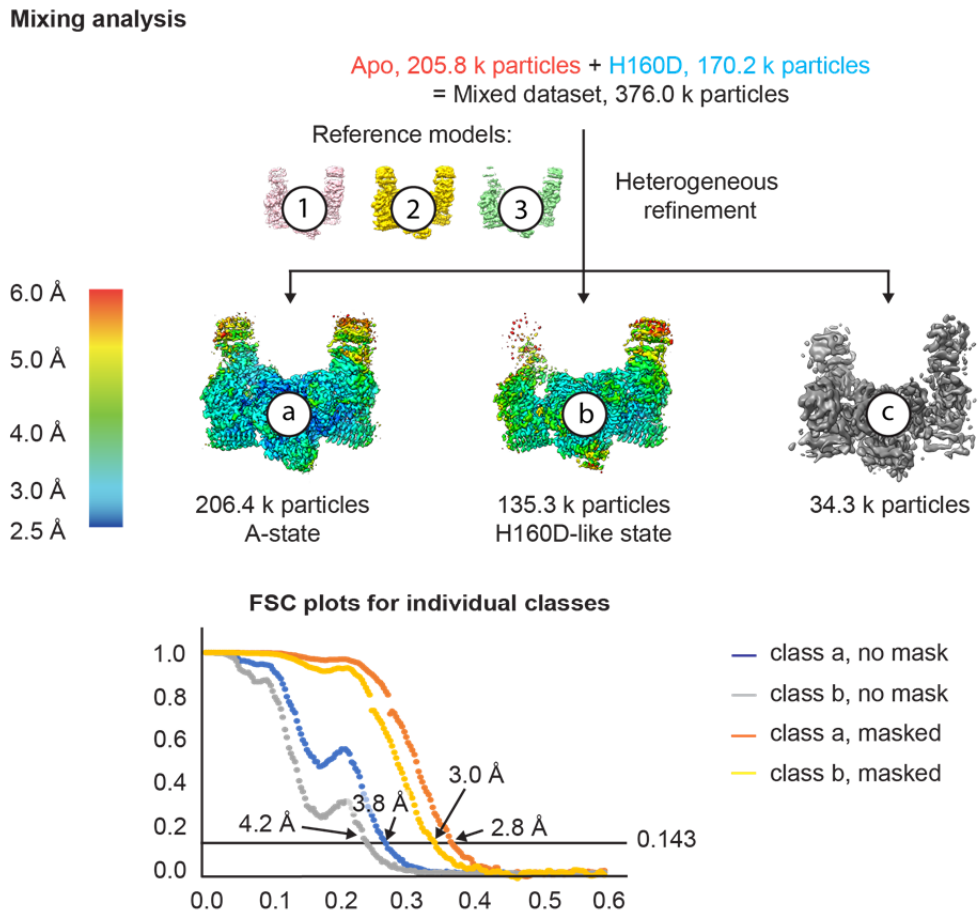

Table Classification result of the mixed dataset

Class	Total number of particles/k	Number of particles from the Apo dataset/k	Percentage of particles from the Apo dataset	Number of particles from the H160D dataset/k	Percentage of particles from the H160D dataset/%
(a)	206.4	156.2	75.9 %	50.3	29.6 %
(b)	135.3	38.2	18.6 %	97.1	57.1 %
(c)	34.3	11.4	5.5 %	22.9	13.5 %

Figure 4 – figure supplement 5. Cryo-EM analysis of the conformation and dynamics of the WT decamer and the βH160D decamer – part 3.

Finally, we performed an extra test to make sure that if a dataset is made up of similar conformations, our cryo-EM analysis is indeed able to separate them into two classes. In this test, we combined particle images from the apo dataset and the H160D dataset and performed heterogeneous refinement using models 1, 2 and 3 from step 1. The results show that most of the particles in the mixed dataset went into one of the two following classes: a class that resembles the classic A-State (class a) and another class that resembles the H160D State (class b). As shown in the table, consistent with the

662 heterogeneous classification results described above, 3D classification of the mixed
663 dataset separated the A- from the I-State, with the majority of A-State particles
664 originating from the apo dataset and the majority of the I-State particles originating from
665 the H160D dataset.
666

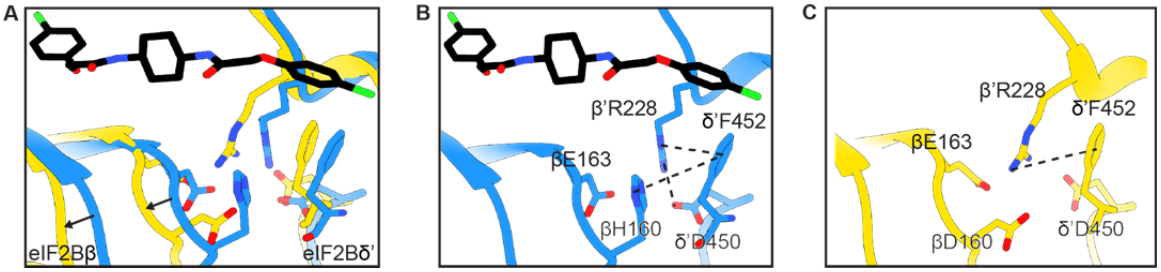

Figure 5 – figures supplement 1. Structural details of the symmetry interface of the WT versus βH160D decamer.

(A) Zoomed-in view of the overlay of the eIF2B$^{\beta H160D}$ structure with the eIF2B-eIF2 structure at the symmetry interface. The βH160D mutation causes the loop bearing βD160 to move away from the opposite tetramer. Black arrows indicate the direction of the movement. (B) Symmetry interface of the eIF2B-eIF2 complex showing the network of interactions. (C) Symmetry interface of the eIF2B$^{\beta H160D}$ structure showing the local structural rearrangements. Each interaction is denoted with a dashed line. eIF2B in the eIF2B-eIF2 complex is colored blue; eIF2B$^{\beta H160D}$ is colored in yellow, and ISRIB in CPK.

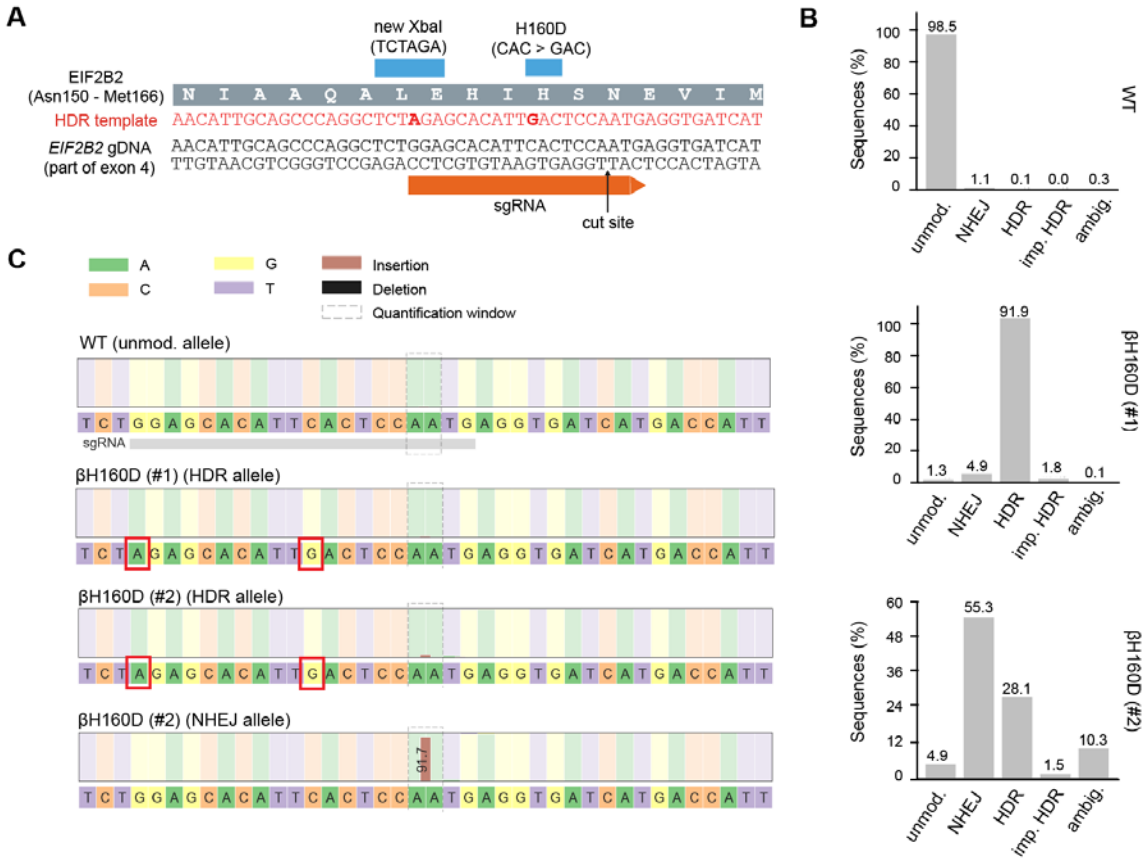

Figure 6 – figure supplement 1. CRISPR-Cas9 editing of the endogenous *EIF2B2* gene with the βH160D mutation in HEK293FTR cells.

(**A**) Editing strategy at target locus of exon 4 in *EIF2B2*. The guide RNA (sgRNA) directs Cas9 for cleavage at a site close to the codon coding for H160. The provided homology-directed repair (HDR) template introduces two basepair substitutions: one for the H160D point mutation (CAC > GAC), and one silent mutation for restriction enzyme mediated clone screening (new XbaI site). gDNA = genomic DNA. (**B, C**) Allele frequencies (B) and sequences (C) at the *EIF2B2* target locus in WT cells and two βH160D clones as determined by deep sequencing. For each cell line, 500,000 randomly-selected sequenced reads were analyzed using the CRISPResso2 pipeline. For one clone, βH160D (#1), >90% of reads matched the HDR template, indicating homozygous editing. For the other clone, βH160D (#2), about 1/3 of reads matched the HDR template, and about 2/3 of reads indicated non-homologous end-joining (NHEJ) with a single A-base insertion, leading to a frameshift mutation and premature translation stop. This suggests this clone is triploidic at the target locus, with a single correctly edited

697 allele and two knock-out alleles. Unmod. = unmodified, imp. = imperfect, ambig. =
698 ambiguous.
699

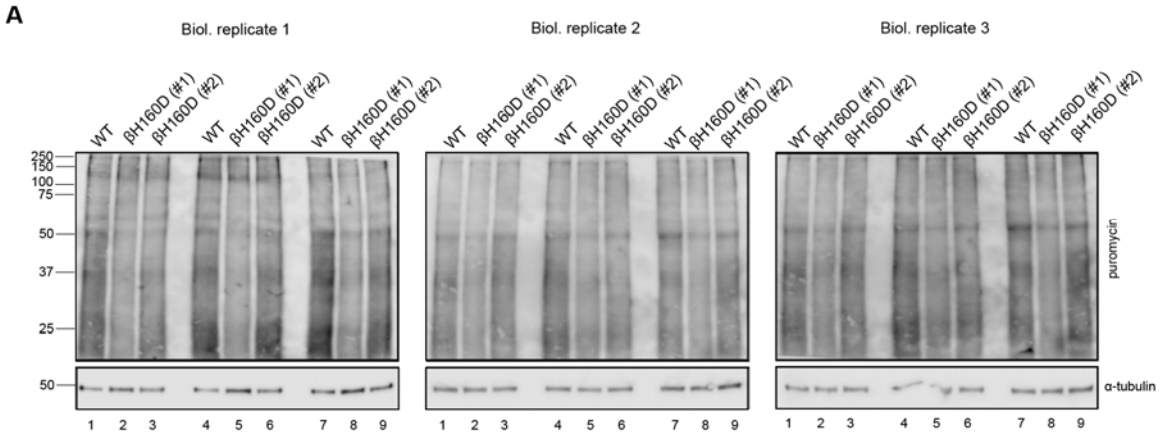

Figure 6 – figure supplement 2. Cells with the βH160D mutation in the endogenous *EIF2B2* gene show reduced protein translation.

Cells were treated for 10 min with puromycin and cell extracts analyzed by polyacrylamide electrophoresis followed by blotting and probing with anti-puromycin (new protein synthesis) or anti-tubulin (loading control) antibodies. Each puromycin incorporation blot represents an independent biological replicate loaded in triplicate to correct for efficiency variations during protein transfer. Equal total protein amounts were loaded in each lane.

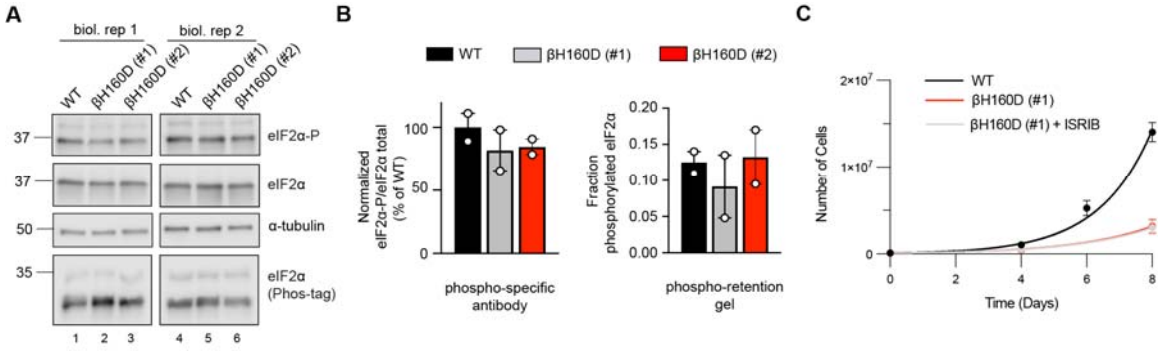

Figure 6 – figure supplement 3. The *EIF2B2*-H160D mutation does not alter phosphorylated eIF2α levels and is ISRIB resistant.

(**A**) Western blot of untreated WT vs *EIF2B2*^{H160D} HEK293FTR cell lines (βH160D (#1) and βH160D (#2)), probing for phospho-eIF2α (S51) (upper row), total eIF2α (middle row), and eIF2α on Phos-tag phospho-retention gel (lower row). Both methods (phospho-specific antibody and phospho-retention on Phostag gels) reveal no major difference in basal phosphorylated eIF2 levels between cell lines. (**B**) Quantification of phosphorylated eIF2α on western blots in (A) using a phospho-specific antibody (left) or on a Phostag gel probed with anti-eIF2α antibody (right). Bars of the left graph represent the mean ratio of eIF2α-P/total eIF2α normalized to WT (n = 2), and differences are not significant (one-way ANOVA with Dunnett post-hoc test, p = 0.53 for WT vs βH160D (#1) and p = 0.61 for WT vs βH160D (#2)). Bars on the right graph represent the mean fraction of eIF2α that migrates slower in the Phostag gel (upper band/(upper band + lower band)) (n = 2). Also here, differences are not significant (one-way ANOVA with Dunnett post-hoc test, p = 0.76 for WT vs βH160D (#1) and p = 0.98 for WT vs βH160D (#2)). (**C**) Growth curves showing that the slow growth of βH160D cells cannot be rescued by ISRIB treatment (n = 3 biological replicates); WT doubling time = 26.8 ± 0.4 h; βH160D (#1) doubling time = 39.6 ± 2.7 h; βH160D (#1) + ISRIB doubling time = 40.2 ± 2.7 h). All error bars and '±' designations are s.e.m.

730
731 **Table 1**

	eIF2 binding				eIF2-P binding		
	WT decamer	**βH160D decamer**	**WT tetramer**		**WT decamer**	**βH160D decamer**	**WT tetramer**
k_a **($M^{-1}s^{-1}$)**	7.0×10^5	8.6×10^5	1.5×10^6		1.1×10^6	2.1×10^6	No binding
k_d **(s^{-1})**	slow: 4.2×10^{-3} fast: 0.12	slow: 5.3×10^{-3} fast: 0.12	0.12		1.5×10^{-2}	1.7×10^{-2}	No binding
K_D **(nM)**	slow: 6.0 fast: 170	slow: 6.1 fast: 140	80		14	8.1	No binding
% slow dissociation	71	33	0		NA	NA	No binding
% fast dissociation	29	67	100		NA	NA	No binding

732
733

734 **Table 2**

Structure	eIF2B$^{\beta H160D}$ (PDB ID: 7TRJ)
Data collection	
Microscope	Titan Krios
Voltage (keV)	300
Nominal magnification	105000x
Exposure navigation	Image shift
Electron dose ($e^{-}Å^{-2}$)	67
Dose rate (e^{-}/pixel/sec)	8
Detector	K3 summit
Pixel size (Å)	0.835
Defocus range (μm)	0.6-2.0
Micrographs	2269
Reconstruction	
Total extracted particles (no.)	1419483
Final particles (no.)	170244
Symmetry imposed	C1
FSC average resolution, masked (Å)	2.8
FSC average resolution, unmasked (Å)	3.8
Applied B-factor (Å)	81.7
Reconstruction package	Cryosparc 2.15
Refinement	
Protein residues	3234
Ligands	0
RMSD Bond lengths (Å)	0.003
RMSD Bond angles (^{o})	0.838
Ramachandran outliers (%)	0.13
Ramachandran allowed (%)	3.62
Ramachandran favored (%)	96.25
Poor rotamers (%)	6.92
CaBLAM outliers (%)	2.50
Molprobity score	2.40
Clash score (all atoms)	9.59
B-factors (protein)	100.54
B-factors (ligands)	N/A
EMRinger Score	2.52
Refinement package	Phenix 1.17.1-3660-000

735

736 **Table 3**

737

Antibody target	Host	Dilution	Manufacturer	Cat. number	Blocking Conditions
eIF2Bβ	Rabbit	1/1,000	ProteinTech	11034-1-AP	PBS-T + 3% milk
eIF2Bε	Mouse	1/1,000	Santa Cruz Biotechnology	sc-55558	PBS-T + 3% milk
ATF4	Rabbit	1/1,000	Cell Signaling	11815S	PBS-T + 3% milk
α-tubulin	Mouse	1/1,000	Cell Signaling	3873T	PBS-T + 3% milk
Puromycin	Mouse	1/10,000	Millipore	MABE343	PBS-T + 3% milk
eIF2α	rabbit	1/1,000	Cell Signaling	5324S	PBS-T + 3% milk
eIF2α-P (S51)	rabbit	1/1,000	Cell Signaling	9721S	PBS-T + 1% BSA

738

739 **Table 4**

Oligo	Sequence	Target gene
B002_F	TGCACCACCAACTGCTTAGC	*GAPDH*
B002_R	GGCATGGACTGTGGTCATGAG	*GAPDH*
D006_F	ATGACCGAAATGAGCTTCCTG	*ATF4*
D006_R	GCTGGAGAACCCATGAGGT	*ATF4*
D007_F	GGAAACAGAGTGGTCATTCCC	*DDIT3 (CHOP)*
D007_R	CTGCTTGAGCCGTTCATTCTC	*DDIT3 (CHOP)*
D070_F	GGAAGACAGCCCCGATTTACT	*ASNS*
D070_R	AGCACGAACTGTTGTAATGTCA	*ASNS*
D073_F	CCATGCAGACTCCACCTTTAC	*CARS*
D073_R	GCAATACCACGTCACCTTTTTC	*CARS*
C001_F	ACTTTAAGCACATTAACCCTG	*EIF2B2*
C001_R	ACTTGATCTTCTCAGTGTCTC	*EIF2B2*
C015	t*G*CAAAACCGTTCTTACAGAAGGGACAATGGAGAACATTGCA GCCCAGGCTCTAGAGCACATTGACTCCAATGAGGTGATCATGA CCATTGGCTTCTCCCGAACAGT	NA (ssODN)
C034_F	CGCGTAATGTGTGTTTGTGA	
C034_R	GCCTCTACTGTTCGGGAGAA	
C036_F_ bc**x**	CAAGCAGAAGACGGCATACGAGAT**xxxxxx**GTGACTGGAGTTCA GACGTGTGCTCTTCCGATCTCGCGTAATGTGTGTTTGTGA	
C036_R	AATGATACGGCGACCACCGAGATCTACACTCTTTCCCTACACG A	
C005_F	acaccgGGAGCACATTCACTCCAATGg	
C005_R	aaaacCATTGGAGTGAATGTGCTCCcg	

740 * phosphorothioate bond.

741 x = barcode nucleotide, different for each clone

742 **Source Data**

743

744 **Figure 1 – source data 1.**

745 Raw data for AUC and FRET experiments. Sed Coeff = sedimentation coefficient.

746

747 **Figure 2 – source data 1.**

748 Raw data for nucleotide exchange assays.

749

750 **Figure 3 – source data 1.**

751 Raw data for SPR assays.

752

753 **Figure 6 – source data 1.**

754 Raw data for the western blots, qPCR, puromycin-incorporation assay, and cell growth.
755 Tg = thapsigargin. 7H9= homozygous βH160D clone (βH160D #1), H11= hemizygous
756 βH160D clone (βH160D #2). Rep = biological replicate.

757

758 **Figure 6 – source data 2.**

759 Original image files for western blots. Tg = thapsigargin. 7H9= homozygous βH160D
760 clone (βH160D #1), H11= hemizygous βH160D clone (βH160D #2).

761

762 **Figure 1 – figure supplement 1 – source data 1**.

763 Original image file for SDS-PAGE gel.

764

765 **Figure 2 – figure supplement 1 – source data 1.**

766 Raw data for Michaelis-Menten analysis of nucleotide exchange at various eIF2
767 concentrations. Rep = replicate.

768

769 **Figure 3 – figure supplement 1 – source data 1.**

770 Raw data for eIF2 binding assessed by SPR using varying association times. Dissoc =
771 dissociation.

772

773 **Figure 6 – figure supplement 2 – source data 1.**

774 Western blots of puromycin incorporation assays. 7H9= homozygous βH160D clone
775 (βH160D #1), H11= hemizygous βH160D clone (βH160D #2). Rep = replicate. Tub =
776 anti-tubulin antibody. Puro = anti-puromycin antibody.
777
778 **Figure 6 – figure supplement 2 – source data 2.**
779 Original image files for western blots of puromycin incorporation assays. 7H9=
780 homozygous βH160D clone (βH160D #1), H11= hemizygous βH160D clone (βH160D
781 #2).
782
783 **Figure 6 – figure supplement 3 – source data 1.**
784 Raw data for the western blots and Phostag blots, and cell growth assay. 7H9=
785 homozygous βH160D clone (βH160D #1), H11= hemizygous βH160D clone (βH160D
786 #2). Rep = biological replicate.
787
788 **Figure 6 – figure supplement 3 – source data 2.**
789 Original image files for western blots of eIF2 phosphorylation status. 7H9= homozygous
790 βH160D clone (βH160D #1), H11= hemizygous βH160D clone (βH160D #2).
791
792
793
794

795 **Materials and Methods**

796

797 **Cloning**

798 *eIF2B2* (encoding eIF2Bβ) and *eIF2B4* (encoding eIF2Bδ) had previously been inserted
799 into sites 1 and 2 of pACYCDuet-1 and then further edited to include mNeonGreen and a
800 $(GGGGS)_2$ linker at the C-terminus of *eIF2B2* and mScarlet-i and a $(GGGGS)_2$ linker at
801 the C-terminus of *eIF2B4* (pMS029). In-Fusion HD cloning was used to edit this plasmid
802 further and insert the H160D mutation into *eIF2B2* (pMS114).

803

804 For CRISPR editing of the *EIF2B2* gene, guide RNAs were designed using the
805 Benchling CRISPR gRNA Design Tool, selecting the guide with the best on-target and
806 off-target scores, and the H160D mutation within 10 bp of the cut site. Cloning of the
807 guide into the guide expression plasmid (MLM3636, with human U6 promoter) was done
808 as previously described (Kwart et al. 2017). In brief, the guide RNA sequence was
809 synthesized as single stranded DNA oligos (C005_F and C005_R) that were first
810 annealed at 2 μM in 1x annealing buffer (40 mM Tris-HCl pH 8.0, 20 mM $MgCl_2$, 50 mM
811 NaCl, 1 mM EDTA pH 8.0), for 5 min at 95°C followed by gradual decrease of -0.1°C/s to
812 25°C. The MLM3636 plasmid was digested using BsmBI (NEB) in NEB Buffer 3.1 for 2 h
813 at 55°C, and the 2.2 kb backbone was isolated from a 0.8% agarose gel with 1x SYBR
814 Safe, and purified using the NucleoSpin Gel and PCR cleanup kit (Macherey Nagel).
815 Backbone and annealed guide template were ligated for 1 h at room temperature using
816 T4 DNA Ligase (NEB), 100 ng backbone, 100 nM guide template, and 1x T4 DNA
817 Ligase buffer (NEB).

818

819 **Purification of human eIF2B subcomplexes**

820 Human eIF2Bα_2 (pJT075), Avi-tagged eIF2Bα_2 (pMS026), WT eIF2Bβγδε (pJT073 and
821 pJT074 co-expression), eIF2Bβ^{H160D}γδε (pJT102 and pJT074), Avi-tagged eIF2Bβγδε
822 (pMS001 and pJT074 co-expression), WT eIF2Bβδγε-F tetramers (pMS029 and pJT074
823 co-expression), and βH160D eIF2Bβδγε-F tetramers (pMS114 and pJT074 co-
824 expression) were purified as previously described (Tsai et al. 2018; Schoof et al. 2021).

825

826 **Purification of heterotrimeric human eIF2**

827 Human eIF2 was purified as previously described (Wong et al. 2018). This material was
828 a generous gift of Calico Life Sciences LLC.

829

830 **Analytical ultracentrifugation**

831 Analytical ultracentrifugation (sedimentation velocity) experiments were performed as
832 previously described using the ProteomeLab XL-I system (Beckman Coulter) (Tsai et al.
833 2018). In brief, samples were loaded into cells in a buffer of 20 mM HEPES-KOH, pH
834 7.5, 150 mM KCl, 1 mM TCEP, and 5 mM $MgCl_2$. A buffer only reference control was
835 also loaded. Samples were then centrifuged in an AN-50 Ti rotor at 40,000 rpm at 20°C
836 and 280 nm absorbance was monitored. Subsequent data analysis was conducted with
837 Sedfit using a non-model-based continuous c(s) distribution.

838

839 ***In vitro* FRET assays**

840 *In vitro* FRET assays were performed as previously described (Schoof et al. 2021).

841

842 **Guanine nucleotide exchange assay**

843 *In vitro* detection of GDP binding to eIF2 was performed as described previously (Schoof
844 et al. 2021). As before, we first monitored the loading of fluorescent BODIPY-FL-GDP to
845 eIF2. Purified human eIF2 (100 nM) was incubated with 100 nM BODIPY-FL-GDP
846 (Thermo Fisher Scientific) in assay buffer (20 mM HEPES-KOH, pH 7.5, 100 mM KCl, 5
847 mM $MgCl_2$, 1 mM TCEP, and 1 mg/ml BSA) to a volume of 18 µl in 384 square-well
848 black-walled, clear-bottom polystyrene assay plates (Corning). For the assay buffer,
849 TCEP and BSA were always freshly added the day of the experiment. For the tetramer
850 GEF assays, a 10X GEF mix was prepared containing 1 µM eIF2Bβγδε tetramer (WT or
851 βH160D), 2% N-methyl-2-pyrrolidone (NMP), and with or without 10 µM ISRIB, again in
852 assay buffer. For the assay, 2 µl of the 10x GEF mix was spiked into the eIF2::BODIPY-
853 FL-GDP mix, bringing the final concentrations to 100 nM tetramer, 0.2% NMP and with
854 or without 1 µM ISRIB. Fluorescence intensity was recorded every 10 s for 40 s prior to
855 the 10X GEF mix spike, and after the spike for 60 min, using a Clariostar PLUS (BMG
856 LabTech) plate reader (excitation wavelength: 477 nm, bandwidth 14 nm; emission
857 wavelength: 525 nm, bandwidth: 30 nm).

858

859 For assays with eIF2B decamers (WT or βH160D), decamers were first assembled by
860 combining eIF2Bβγδε tetramer (WT or βH160D) with eIF2Bα_2 dimer in a 1:1 molar ratio
861 (a 2-fold excess of eIF2Bα_2 dimer compared to the number of eIF2B$(\beta\gamma\delta\varepsilon)_2$ octamers) at
862 room temperature for at least 30 min. The 10X GEF mix for decamer assays contained

863 100 nM eIF2B(αβγδε)$_2$ decamer (WT or βH160D) in assay buffer. The ensuing steps
864 were performed as described for the GEF assays with tetramers. Immediately after the
865 loading assay, in the same wells, we spiked in unlabeled GDP to 1 mM to measure
866 unloading, again recording fluorescence intensities every 10s for 60 min as before.
867 These data were fit to a first-order exponential. For clarity, datapoints were averaged at
868 1 min intervals and then plotted as single datapoints in Figure 2.
869
870 **Michaelis-Menten kinetics**
871 The Michaelis-Menten kinetic analysis of eIF2B(αβγδε)$_2$ decamer (WT or βH160D) GEF
872 activity was performed as described previously, with some minor modifications (Schoof
873 et al. 2021). Briefly, BODIPY-FL-GDP loading assays were performed as described
874 above, keeping final decamer concentrations at 10 nM, but varying substrate
875 concentration from 0 nM to 4 μM. BODIPY-FL-GDP concentration was kept at 2 μM
876 final. The initial velocity was determined by a linear fit to timepoints acquired at 5 s
877 intervals from 50 to 200 s after addition of decamer. To convert fluorescence intensities
878 to pmol substrate, the gain in signal after 60 min was plotted against eIF2 concentration
879 for the 31.5 nM – 1 μM concentrations. V_{max} and K_M were determined by fitting the initial
880 velocities as a function of eIF2 concentration to the Michaelis–Menten equation in
881 GraphPad Prism 9. For statistical comparisons of V_{max} and K_M, we used a two-sided t-
882 test with α = 0.05, comparing V_{max} or K_M derived from the individual fit of each replicate
883 experiment.
884
885 **Affinity determination and variable association analysis by surface plasmon**
886 **resonance**
887 eIF2 and eIF2-P affinity determination experiments were performed on a Biacore T200
888 instrument (Cytiva Life Sciences) by capturing the biotinylated WT eIF2B decamer,
889 βH160D eIF2B decamer, and WT eIF2B tetramer at ~50nM on a Biotin CAPture Series
890 S sensor chip (Cytiva Life Sciences) to achieve maximum response (Rmax) of under
891 ~150 response units (RUs) upon eIF2 or eIF2-P binding. eIF2-P was prepared by mixing
892 5 μM eIF2 in 50-fold excess of 100 nM PERK kinase and with 1 mM ATP. The mixture
893 was incubated at room temperature for 60 min before incubation on ice until dilution into
894 the titration series. 2-fold serial dilutions of purified eIF2 or eIF2-P were flowed over the
895 captured eIF2B complexes at 30 μl / min for 60 seconds followed by 600 seconds of
896 dissociation flow. Following each cycle, the chip surface was regenerated with 3 M

897 guanidine hydrochloride. A running buffer of 20 mM HEPES-KOH, pH 7.5, 100 mM KCl,
898 5 mM $MgCl_2$, and 1 mM TCEP was used throughout. The resulting sensorgrams were fit
899 in GraphPad Prism 8.0. Association was fit for all species using the association then
900 dissociation model. For eIF2-P binding this model was used to fit dissociation as well.
901 For eIF2 binding, dissociation was fit using the two phase decay model. For eIF2 binding
902 to WT tetramer the data could be modeled with one phase association, one phase
903 dissociation kinetics by setting the percent fast phase dissociation to 100%. For variable
904 association experiments, WT and βH160D eIF2B decamer was immobilized as
905 described above. A solution containing 62.5 nM eIF2 was flowed over the captured
906 eIF2B for 5-480 s at 30 µl / min to reach the equilibrium of % fast phase dissociation vs
907 % slow phase dissociation. Association was followed by 480 seconds of dissociation
908 flow. The dissociation phase was then fit in GraphPad Prism 8.0 using the two phase
909 decay model as described above.
910
911 **Generation of endogenous βH160D cells**
912 Editing of the *EIF2B2* gene to introduce the H160D mutation in HEK293Flp-In TRex
913 (HEK293FTR) cells was performed using CRISPR-Cas9 according to a previously
914 published protocol, with some minor modifications (Kwart et al. 2017). Cells were
915 seeded at 250,000 cells/well of a 12-well plate and grown for 24 h prior to transfection
916 with a PAGE-purified, phosphorothioate-protected single-stranded oligonucleotide donor
917 (ssODN) for homologous recombination (C015) (Renaud et al. 2016), a plasmid
918 containing Cas9-GFP, and a plasmid encoding the guide RNA (MLM3636-C005). The
919 100 nt ssODN was designed to simultaneously introduce the H160D missense mutation
920 (CAC to GAC), to add a silent XbaI restriction site at L156 (TCTGGA to TCTAGA), and
921 to block re-digestion by Cas9 after recombination. Transfection was done with Xtreme
922 Gene9 reagent according to the manufacturer's protocol, using a 3:1 ratio of reagent (µl)
923 to DNA (µg). Reagent-only and pCas9-GFP controls were included. Two days post
924 transfection, cells were trypsinized, washed twice in ice-cold filter-sterilized FACS buffer
925 (25 mM HEPES pH 7.0, 2 mM EDTA, 0.5% v/v fetal bovine serum, in 1x PBS), and
926 resuspended in FACS buffer with 400 ng/ml 7-AAD viability dye (Invitrogen) at around 1
927 million cells/ml in filter-capped FACS tubes. Single GFP^+, 7-AAD^- cells were sorted into
928 recovery medium (a 1:1 mix of conditioned medium, and fresh medium with 20% fetal
929 bovine serum, 2 mM L-Glutamine, 1 mM sodium pyruvate, and 1x non-essential amino
930 acids) in single wells of 96-well plates using the Sony SH800 cell sorter. The survival

931 rate was around 2% after 2-3 weeks. Surviving clones were expanded and first screened
932 for correct editing by PCR and XbaI restriction digest. For this, genomic DNA was
933 isolated using the PureLink Genomic DNA mini kit (Invitrogen), and a 473 bp fragment of
934 the *EIF2B2* gene was amplified by PCR using 300 nM forward and reverse primers
935 (C001_F and C001_R), 300 µM dNTPs, 1x HF buffer, 100 ng genomic DNA / 100 µl
936 reaction and 2 U/100 µl reaction of KAPA HiFi polymerase for 3 min at 95°C; and 30
937 cycles of 98°C for 20 s, 68.9°C for 15 s, 72°C for 15 s, prior to cooling at 4°C. PCR
938 reactions were purified using NucleoSpin Gel and PCR cleanup kit (Macherey Nagel),
939 and HighPrep PCR Cleanup beads (MagBio Genomics) using the manufacturer's
940 instructions. Cleaned up products were digested using XbaI restriction enzyme (NEB) in
941 1x CutSmart buffer and run on a 1.5% agarose gel with 1x SYBR Safe (Invitrogen) and
942 100 bp DNA ladder (Promega). Clones with an XbaI restriction site were then deep
943 sequenced to confirm correct editing and zygosity. For this, the *EIF2B2* gene was
944 amplified by PCR using 300 nM forward and reverse primers (C034_F and C034_R),
945 300 µM dNTPs, 1x HF buffer, 100 ng genomic DNA / 100 µl reaction and 2 U/100 µl
946 reaction of KAPA HiFi polymerase for 3 min at 95°C; and 30 cycles of 98°C for 20 s,
947 64.9°C for 15 s, 72°C for 15 s, prior to cooling at 4°C. The 196 bp product was purified
948 from a 1.5% agarose gel with 1x SYBR Safe using NucleoSpin Gel and PCR cleanup kit
949 (Macherey Nagel), and HighPrep PCR Cleanup beads (MagBio Genomics) using the
950 manufacturer's instructions. A subsequent second PCR added the Illumina P5/P7
951 sequences and barcode for deep sequencing. For this, we used 15 ng purified PCR
952 product per 100 µl reaction, 300 nM forward and reverse primer (C036_F_bcx, and
953 C036_R), and 1x KAPA HiFi HotStart mix, for 3 min at 95°C, and 8 cycles of 20 s at
954 98°C, 15 s at 63.7°C, and 15 s at 72°C prior to cooling on ice. PCR reactions were
955 purified using HighPrep beads (MagBio Genomics), and amplicon quality and size
956 distribution was checked by chip electrophoresis (BioAnalyzer High Sensitivity kit,
957 Agilent). Samples were then sequenced on an Illumina MiSeq (150 bp paired-end), and
958 results were analyzed with CRISPResso (Pinello et al. 2016). All cell lines were negative
959 for mycoplasma contamination. Amplicon sequencing data was deposited in NCBI's
960 Sequence Read Archive (SRA) under accession number PRJNA821864.
961 .
962
963 **Growth Curves**

964 Cells were seeded at 100,000 cells/well of a 6-well plate and grown at 37°C and 5%
965 CO_2. At confluency, cells were trypsinized, expanded into larger plates, and counted.
966 This was repeated until the WT cells reached confluency in a T225 flask. For drug
967 treatment conditions (Figure 6 – figure supplement 3C), we used 500 nM ISRIB with
968 DMSO at a final concentration of 0.1% across conditions.
969
970 **Western Blotting**
971 Cells were seeded at 400,000 cells/well of a 6-well plate and grown at 37°C and 5% CO_2
972 for 24 h. For drug treatment, we used 10 nM thapsigargin (Tg) (Invitrogen) and 200 nM
973 ISRIB (made in-house) for 1 h, ensuring the final DMSO concentration was 0.1% across
974 all conditions. For the protein synthesis assay, puromycin was added to a final
975 concentration of 10 µg/ml for 10 min. Plates were put on ice, cells were washed once
976 with ice-cold phosphate-buffered saline (PBS), and then lysed in 150 µl ice-cold lysis
977 buffer (50 mM Tris-HCl pH 7.4, 150 mM NaCl, 1 mM EDTA, 1% v/v Triton X-100, 10%
978 v/v glycerol, 1x cOmplete protease inhibitor cocktail [Roche], and 1x PhosSTOP
979 [Roche]). Cells were scraped off, collected in an eppendorf tube, and put on a rotator for
980 30 min at 4°C. Debris was pelleted at 12,000 g for 20 min at 4°C, and supernatant was
981 removed to a new tube on ice. Protein concentration was measured using the
982 bicinchonic acid (BCA) assay. Within an experiment, total protein concentration was
983 normalized to the least concentrated sample (typically all values were within ~10%). A 5x
984 Laemmli loading buffer (250 mM Tris-HCl pH 6.8, 30% glycerol, 0.25% bromophenol
985 blue, 10% SDS, 5% β-mercaptoethanol) was added to each sample to 1x, and samples
986 were denatured at 95°C for 12 min, then cooled on ice. Wells of AnyKd Mini-PROTEAN
987 TGX precast protein gels (AnyKD, Bio-Rad) were loaded with equal amounts of total
988 protein (around 10 µg), in between Precision Plus Dual Color protein ladder (BioRad).
989 After electrophoresis, proteins were transferred onto a nitrocellulose membrane at 4°C,
990 and then blocked for 2 h at room temperature in PBS with 0.1% Tween (PBS-T) + 3%
991 milk (blocking buffer) while rocking. Primary antibody staining was performed with gentle
992 agitation at 4°C overnight using the conditions outlined in Table 3. After washing four
993 times in blocking buffer, secondary antibody staining was performed for 1 h at room
994 temperature using anti-rabbit HRP or anti-mouse HRP secondary antibodies (Promega,
995 1:10,000) in blocking buffer. Membranes were washed 3x in blocking buffer and then 1x
996 in PBS-T without milk. Chemiluminescent detection was performed using SuperSignal

997 West Dura or Femto HRP substrate (Thermo Fisher Scientific), and membranes were
998 imaged on a LI-COR Odyssey gel imager for 0.5–10 min depending on band intensity.
999
1000 For the phospho-retention blots, equal amounts of total protein lysates (around 10 µg)
1001 were loaded on 12.5% Supersep Phos-tag gels (Wako Chemicals) in between Wide-
1002 view III protein ladder (Wako Chemicals). After electrophoresis, the gel was washed 3x
1003 in transfer buffer with 10 mM EDTA prior to transfer onto nitrocellulose. Blocking,
1004 antibody staining and detection was performed as described above.
1005
1006 **RT-qPCR**
1007 Cells were seeded at 400,000 cells/well of a 12-well plate and grown at 37°C and 5%
1008 CO_2 for 24 h. The day of RNA extraction, medium was removed, and cells were lysed in
1009 350 µl TriZOL reagent (Invitrogen). All further handling was done in a fume hood
1010 decontaminated for the presence of RNAses using RNAse ZAP (Invitrogen). Total RNA
1011 was isolated using the DirectZOL RNA miniprep kit (Zymo Research), including an on-
1012 column DNase digest, according to the manufacturer's instructions. RNA concentration
1013 was measured using Nanodrop. cDNA was synthesized using 600 ng input total RNA
1014 per 40 µl reaction with the iScript cDNA Synthesis Kit (BioRad), cycling for 5 min at
1015 25°C, 20 min at 46°C, and 1 min at 95°C. Samples were cooled and diluted 1/5 in
1016 Rnase-free water. qPCR reactions were set up with final 1x iQ SYBR Green supermix
1017 (BioRad), 400 nM each of Fw and Rev QPCR primers (see Table 4), 1/5 of the diluted
1018 cDNA reaction, and RNAse-free water. No-template and no-reverse transcription
1019 reactions were included as controls. Reactions were run in triplicates as 10 µl reactions
1020 in 384-well plates on a BioRad CFX384 Thermocycler, for 3 min at 95°C, and then 40
1021 cycles of 95°C for 10 s and 60°C for 30 s, ending with heating from 55°C to 95°C in
1022 0.5°C increments for melting curve generation. C_qs and melting curves were calculated
1023 by the BioRad software. C_q values of technical replicates were averaged, and values
1024 were calculated with the ΔΔCt method using *GAPDH* for reference gene normalization.
1025 Graph points reflect fold changes compared to WT vehicle, with bars being the mean +/-
1026 s.e.m. Statistical analysis was done using GraphPad Prism 9 on log-transformed values
1027 with ordinary one-way ANOVA and Dunnett's post-hoc test.
1028
1029 **Sample preparation for cryo-electron microscopy**

1030 Decameric eIF2Bβ^{H160D} was prepared by incubating 16 μM eIF2Bβ^{H160D}γδε with 8.32 μM
1031 eIF2Bα$_2$ in a final solution containing 20 mM HEPES-KOH, 200 mM KCl, 5 mM $MgCl_2$,
1032 and 1 mM TCEP. This 8 μM eIF2B(αβ^{H160D}γδε)$_2$ sample was further diluted to 750 nM.
1033 For grid freezing, a 3 μl aliquot of the sample was applied onto the Quantifoil R 1.2/1/3
1034 400 mesh Gold grid and we waited for 30 s. A 0.5 μl aliquot of 0.1-0.2% Nonidet P-40
1035 substitute was added immediately before blotting. The entire blotting procedure was
1036 performed using Vitrobot (FEI) at 10 ºC and 100% humidity.
1037
1038 **Electron microscopy data collection**
1039 Cryo-EM data was collected on a Titan Krios transmission electron microscope
1040 operating at 300 keV. Micrographs were acquired using a Gatan K3 direct electron
1041 detector. The total dose was 67 e^-/ Å^2, and 117 frames were recorded during a 5.9 s
1042 exposure. Data was collected at 105,000 x nominal magnification (0.835 Å/pixel at the
1043 specimen level), with a nominal defocus range of -0.6 to -2.0 μm.
1044
1045 **Image processing**
1046 The micrograph frames were aligned using MotionCor2 (Zheng et al. 2017). The contrast
1047 transfer function (CTF) parameters were estimated with GCTF (Zhang 2016). For the
1048 decameric eIF2B^{βH160D}, Particles were picked in Cryosparc v2.15 using the apo eIF2B
1049 (EMDB: 23209) as a template (Punjani et al. 2017; Schoof et al. 2021). Particles were
1050 extracted using an 80-pixel box size and classified in 2D. Classes that showed clear
1051 protein features were selected and extracted for ab initio reconstruction, followed by
1052 homogenous refinement. Particles belonging to the best class were then re-extracted
1053 with a pixel size of 2.09 Å, and then subjected to homogeneous refinement, yielding a
1054 reconstruction of 4.25 Å. These particles were subjected to another round of
1055 heterogeneous refinement followed by homogeneous refinement to generate a
1056 consensus reconstruction consisting of the best particles. These particles were re-
1057 extracted at a pixel size of 0.835 Å. Then, CTF refinement was performed to correct for
1058 the per-particle CTF as well as beam tilt. A final round of nonuniform refinement yielded
1059 the final structure of 2.8 Å.
1060
1061 **Atomic model building, refinement, and visualization**
1062 For the decameric eIF2B^{βH160D}, the previously published apo eIF2B model (PDB ID:
1063 7L70) was used as a starting model (Schoof et al. 2021). Each subunit was docked into

1064 the EM density individually and then subjected to rigid body refinement in Phenix
1065 (Adams et al. 2010). The models were then manually adjusted in Coot and then refined
1066 in phenix.real_space_refine using global minimization, secondary structure restraints,
1067 Ramachandran restraints, and local grid search (Emsley and Cowtan 2004). Then
1068 iterative cycles of manual rebuilding in Coot and phenix.real_space_refine were
1069 performed. The final model statistics were tabulated using Molprobity (Chen et al. 2010).
1070 Distances were calculated from the atomic models using UCSF Chimera (Pettersen et
1071 al. 2004). Molecular graphics and analyses were performed with the UCSF Chimera
1072 package. UCSF Chimera is developed by the Resource for Biocomputing, Visualization,
1073 and Informatics and is supported by NIGMS P41-GM103311. The atomic model is
1074 deposited into PDB under the accession code 7TRJ. The EM map is deposited into
1075 EMDB under the accession code EMD-26098.
1076

1077 **Acknowledgments**
1078 We thank the Walter lab for helpful discussions throughout this project; Geeta Narlikar
1079 for input on enzyme kinetics; Calico for a generous gift of purified eIF2 heterotrimer; and
1080 Z Yu and D Bulkley of the UCSF Center for Advanced Cryo-EM facility, which is
1081 supported by NIH grants S10OD021741 and S10OD020054 and the Howard Hughes
1082 Medical Institute (HHMI); We also thank the QB3 shared cluster for computational
1083 support and Hehua and Quixote for inspiration and emotional support.
1084

1085 **Funding**
1086 This work was supported by generous support from Calico Life Sciences LLC (to PW); a
1087 generous gift from The George and Judy Marcus Family Foundation (To PW); the
1088 Belgian-American Educational Foundation (BAEF) Postdoctoral Fellowship (to MB), the
1089 Damon Runyon Cancer Research Foundation Postdoctoral fellowship (to LW); the Jane
1090 Coffin Child Foundation Postdoctoral Fellowship (to RL); a Chan Zuckerberg Biohub
1091 Investigator award and an HHMI Faculty Scholar grant (AF). PW is an Investigator of the
1092 Howard Hughes Medical Institute.
1093

1094 **Competing Interests**
1095 PW is an inventor on U.S. Patent 9708247 held by the Regents of the University of
1096 California that describes ISRIB and its analogs. Rights to the invention have been

licensed by UCSF to Calico. For the remaining authors, no competing financial interests exist.

1099 **References**
1100

1101 Abdulkarim, B., M. Nicolino, M. Igoillo-Esteve, M. Daures, S. Romero, A. Philippi, V.
1102 Senée, M. Lopes, D. A. Cunha, H. P. Harding, C. Derbois, N. Bendelac, A. T.
1103 Hattersley, D. L. Eizirik, D. Ron, M. Cnop, and C. Julier. 2015. 'A Missense
1104 Mutation in PPP1R15B Causes a Syndrome Including Diabetes, Short Stature,
1105 and Microcephaly', *Diabetes*, 64: 3951-62.
1106 Adams, P. D., P. V. Afonine, G. Bunkóczi, V. B. Chen, I. W. Davis, N. Echols, J. J. Headd,
1107 L. W. Hung, G. J. Kapral, R. W. Grosse-Kunstleve, A. J. McCoy, N. W. Moriarty, R.
1108 Oeffner, R. J. Read, D. C. Richardson, J. S. Richardson, T. C. Terwilliger, and P.
1109 H. Zwart. 2010. 'PHENIX: a comprehensive Python-based system for
1110 macromolecular structure solution', *Acta Crystallogr D Biol Crystallogr*, 66:
1111 213-21.
1112 Adomavicius, T., M. Guaita, Y. Zhou, M. D. Jennings, Z. Latif, A. M. Roseman, and G. D.
1113 Pavitt. 2019. 'The structural basis of translational control by eIF2
1114 phosphorylation', *Nat Commun*, 10: 2136.
1115 Algire, M. A., D. Maag, and J. R. Lorsch. 2005. 'Pi release from eIF2, not GTP
1116 hydrolysis, is the step controlled by start-site selection during eukaryotic
1117 translation initiation', *Mol Cell*, 20: 251-62.
1118 Bogorad, A. M., K. Y. Lin, and A. Marintchev. 2017. 'Novel mechanisms of eIF2B
1119 action and regulation by eIF2α phosphorylation', *Nucleic Acids Res*, 45:
1120 11962-79.
1121 Chen, V. B., W. B. Arendall, 3rd, J. J. Headd, D. A. Keedy, R. M. Immormino, G. J. Kapral,
1122 L. W. Murray, J. S. Richardson, and D. C. Richardson. 2010. 'MolProbity: all-
1123 atom structure validation for macromolecular crystallography', *Acta*
1124 *Crystallogr D Biol Crystallogr*, 66: 12-21.
1125 Chou, A., K. Krukowski, T. Jopson, P. J. Zhu, M. Costa-Mattioli, P. Walter, and S. Rosi.
1126 2017. 'Inhibition of the integrated stress response reverses cognitive deficits
1127 after traumatic brain injury', *Proc Natl Acad Sci U S A*, 114: E6420-e26.
1128 Costa-Mattioli, M., and P. Walter. 2020. 'The integrated stress response: From
1129 mechanism to disease', *Science*, 368: eaat5314.
1130 Dey, M., C. Cao, A. C. Dar, T. Tamura, K. Ozato, F. Sicheri, and T. E. Dever. 2005.
1131 'Mechanistic link between PKR dimerization, autophosphorylation, and
1132 eIF2alpha substrate recognition', *Cell*, 122: 901-13.
1133 Emsley, P., and K. Cowtan. 2004. 'Coot: model-building tools for molecular graphics',
1134 *Acta Crystallogr D Biol Crystallogr*, 60: 2126-32.
1135 Gordiyenko, Y., J. L. Llácer, and V. Ramakrishnan. 2019. 'Structural basis for the
1136 inhibition of translation through eIF2α phosphorylation', *Nat Commun*, 10:
1137 2640.
1138 Gordiyenko, Y., C. Schmidt, M. D. Jennings, D. Matak-Vinkovic, G. D. Pavitt, and C. V.
1139 Robinson. 2014. 'eIF2B is a decameric guanine nucleotide exchange factor
1140 with a γ2ε2 tetrameric core', *Nat Commun*, 5: 3902.
1141 Guo, X., G. Aviles, Y. Liu, R. Tian, B. A. Unger, Y. T. Lin, A. P. Wiita, K. Xu, M. A. Correia,
1142 and M. Kampmann. 2020. 'Mitochondrial stress is relayed to the cytosol by an
1143 OMA1-DELE1-HRI pathway', *Nature*, 579: 427-32.

1144 Hao, Q., J. M. Heo, B. P. Nocek, K. G. Hicks, V. S. Stoll, C. Remarcik, S. Hackett, L. LeBon,
1145 R. Jain, D. Eaton, J. Rutter, Y. L. Wong, and C. Sidrauski. 2021. 'Sugar
1146 phosphate activation of the stress sensor eIF2B', *Nat Commun*, 12: 3440.
1147 Harding, H. P., I. Novoa, Y. Zhang, H. Zeng, R. Wek, M. Schapira, and D. Ron. 2000.
1148 'Regulated translation initiation controls stress-induced gene expression in
1149 mammalian cells', *Mol Cell*, 6: 1099-108.
1150 Harding, H. P., H. Zeng, Y. Zhang, R. Jungries, P. Chung, H. Plesken, D. D. Sabatini, and
1151 D. Ron. 2001. 'Diabetes mellitus and exocrine pancreatic dysfunction in perk-
1152 /- mice reveals a role for translational control in secretory cell survival', *Mol*
1153 *Cell*, 7: 1153-63.
1154 Hinnebusch, A. G. 2005. 'Translational regulation of GCN4 and the general amino
1155 acid control of yeast', *Annu Rev Microbiol*, 59: 407-50.
1156 Hinnebusch, A. G., I. P. Ivanov, and N. Sonenberg. 2016. 'Translational control by 5'-
1157 untranslated regions of eukaryotic mRNAs', *Science*, 352: 1413-6.
1158 Kashiwagi, K., M. Takahashi, M. Nishimoto, T. B. Hiyama, T. Higo, T. Umehara, K.
1159 Sakamoto, T. Ito, and S. Yokoyama. 2016. 'Crystal structure of eukaryotic
1160 translation initiation factor 2B', *Nature*, 531: 122-5.
1161 Kashiwagi, K., T. Yokoyama, M. Nishimoto, M. Takahashi, A. Sakamoto, M.
1162 Yonemochi, M. Shirouzu, and T. Ito. 2019. 'Structural basis for eIF2B
1163 inhibition in integrated stress response', *Science*, 364: 495-99.
1164 Kashiwagi, K., Y. Shichino, T. Osaki, A. Sakamoto, M. Nishimoto, M. Takahashi, M.
1165 Mito, F. Weber, Y. Ikeuchi, S. Iwasaki, and T. Ito. 2021. 'eIF2B-capturing viral
1166 protein NSs suppresses the integrated stress response', *Nat Commun,* 12:
1167 7102.
1168 Kenner, L. R., A. A. Anand, H. C. Nguyen, A. G. Myasnikov, C. J. Klose, L. A. McGeever, J.
1169 C. Tsai, L. E. Miller-Vedam, P. Walter, and A. Frost. 2019. 'eIF2B-catalyzed
1170 nucleotide exchange and phosphoregulation by the integrated stress
1171 response', *Science*, 364: 491-95.
1172 Konieczny, A., and B. Safer. 1983. 'Purification of the eukaryotic initiation factor 2-
1173 eukaryotic initiation factor 2B complex and characterization of its guanine
1174 nucleotide exchange activity during protein synthesis initiation', *J Biol Chem*,
1175 258: 3402-8.
1176 Koromilas, A. E., S. Roy, G. N. Barber, M. G. Katze, and N. Sonenberg. 1992. 'Malignant
1177 transformation by a mutant of the IFN-inducible dsRNA-dependent protein
1178 kinase', *Science*, 257: 1685-9.
1179 Krukowski, K., A. Nolan, E. S. Frias, M. Boone, G. Ureta, K. Grue, M. S. Paladini, E.
1180 Elizarraras, L. Delgado, S. Bernales, P. Walter, and S. Rosi. 2020. 'Small
1181 molecule cognitive enhancer reverses age-related memory decline in mice',
1182 *Elife*, 9: e62048
1183 Kwart, D., D. Paquet, S. Teo, and M. Tessier-Lavigne. 2017. 'Precise and efficient
1184 scarless genome editing in stem cells using CORRECT', *Nat Protoc*, 12: 329-
1185 54.
1186 Leegwater, P. A., G. Vermeulen, A. A. Könst, S. Naidu, J. Mulders, A. Visser, P.
1187 Kersbergen, D. Mobach, D. Fonds, C. G. van Berkel, R. J. Lemmers, R. R. Frants,
1188 C. B. Oudejans, R. B. Schutgens, J. C. Pronk, and M. S. van der Knaap. 2001.

1189 'Subunits of the translation initiation factor eIF2B are mutant in
1190 leukoencephalopathy with vanishing white matter', *Nat Genet*, 29: 383-8.
1191 Li, W., X. Wang, M. S. Van Der Knaap, and C. G. Proud. 2004. 'Mutations linked to
1192 leukoencephalopathy with vanishing white matter impair the function of the
1193 eukaryotic initiation factor 2B complex in diverse ways', *Mol Cell Biol*, 24:
1194 3295-306.
1195 Lu, P. D., H. P. Harding, and D. Ron. 2004. 'Translation reinitiation at alternative open
1196 reading frames regulates gene expression in an integrated stress response', *J*
1197 *Cell Biol*, 167: 27-33.
1198 Lu, Y. N., S. Kavianpour, T. Zhang, X. Zhang, D. Nguyen, R. Thombre, L. He, and J.
1199 Wang. 2021. 'MARK2 phosphorylates eIF2α in response to proteotoxic
1200 stress', *PLoS Biol*, 19: e3001096.
1201 Ma, T., M. A. Trinh, A. J. Wexler, C. Bourbon, E. Gatti, P. Pierre, D. R. Cavener, and E.
1202 Klann. 2013. 'Suppression of eIF2α kinases alleviates Alzheimer's disease-
1203 related plasticity and memory deficits', *Nat Neurosci*, 16: 1299-305.
1204 Matts, R. L., D. H. Levin, and I. M. London. 1983. 'Effect of phosphorylation of the
1205 alpha-subunit of eukaryotic initiation factor 2 on the function of reversing
1206 factor in the initiation of protein synthesis', *Proc Natl Acad Sci U S A*, 80:
1207 2559-63.
1208 Nguyen, H. G., C. S. Conn, Y. Kye, L. Xue, C. M. Forester, J. E. Cowan, A. C. Hsieh, J. T.
1209 Cunningham, C. Truillet, F. Tameire, M. J. Evans, C. P. Evans, J. C. Yang, B.
1210 Hann, C. Koumenis, P. Walter, P. R. Carroll, and D. Ruggero. 2018.
1211 'Development of a stress response therapy targeting aggressive prostate
1212 cancer', *Sci Transl Med*, 10: eaar2036
1213 Pettersen, E. F., T. D. Goddard, C. C. Huang, G. S. Couch, D. M. Greenblatt, E. C. Meng,
1214 and T. E. Ferrin. 2004. 'UCSF Chimera--a visualization system for exploratory
1215 research and analysis', *J Comput Chem*, 25: 1605-12.
1216 Pinello, L., M. C. Canver, M. D. Hoban, S. H. Orkin, D. B. Kohn, D. E. Bauer, and G. C.
1217 Yuan. 2016. 'Analyzing CRISPR genome-editing experiments with
1218 CRISPResso', *Nat Biotechnol*, 34: 695-7.
1219 Punjani, A., J. L. Rubinstein, D. J. Fleet, and M. A. Brubaker. 2017. 'cryoSPARC:
1220 algorithms for rapid unsupervised cryo-EM structure determination', *Nat*
1221 *Methods*, 14: 290-96.
1222 Renaud, J. B., C. Boix, M. Charpentier, A. De Cian, J. Cochennec, E. Duvernois-Berthet,
1223 L. Perrouault, L. Tesson, J. Edouard, R. Thinard, Y. Cherifi, S. Menoret, S.
1224 Fontanière, N. de Crozé, A. Fraichard, F. Sohm, I. Anegon, J. P. Concordet, and
1225 C. Giovannangeli. 2016. 'Improved Genome Editing Efficiency and Flexibility
1226 Using Modified Oligonucleotides with TALEN and CRISPR-Cas9 Nucleases',
1227 *Cell Rep*, 14: 2263-72.
1228 Rowlands, A. G., R. Panniers, and E. C. Henshaw. 1988. 'The catalytic mechanism of
1229 guanine nucleotide exchange factor action and competitive inhibition by
1230 phosphorylated eukaryotic initiation factor 2', *J Biol Chem*, 263: 5526-33.
1231 Salimans, M., H. Goumans, H. Amesz, R. Benne, and H. O. Voorma. 1984. 'Regulation
1232 of protein synthesis in eukaryotes. Mode of action of eRF, an eIF-2-recycling
1233 factor from rabbit reticulocytes involved in GDP/GTP exchange', *Eur J*
1234 *Biochem*, 145: 91-8.

1235 Schoof, M., M. Boone, L. Wang, R. Lawrence, A. Frost, and P. Walter. 2021. 'eIF2B
1236 conformation and assembly state regulate the integrated stress response',
1237 *Elife*, 10: e65703.
1238 Schoof, M., L. Wang, J. Z. Cogan, R. Lawrence, M. Boone, J. D. Wuerth, A. Frost, and P.
1239 Walter. 2021. 'Viral Evasion of the Integrated Stress Response Through
1240 Antagonistic eIF2-P Mimicry', *Nat Commun,* 12: 7103.
1241 Sekine, Y., A. Zyryanova, A. Crespillo-Casado, P. M. Fischer, H. P. Harding, and D. Ron.
1242 2015. 'Stress responses. Mutations in a translation initiation factor identify
1243 the target of a memory-enhancing compound', *Science*, 348: 1027-30.
1244 Sen, T., R. Gupta, H. Kaiser, and N. Sen. 2017. 'Activation of PERK Elicits Memory
1245 Impairment through Inactivation of CREB and Downregulation of PSD95
1246 After Traumatic Brain Injury', *J Neurosci*, 37: 5900-11.
1247 Shi, Y., K. M. Vattem, R. Sood, J. An, J. Liang, L. Stramm, and R. C. Wek. 1998.
1248 'Identification and characterization of pancreatic eukaryotic initiation factor
1249 2 alpha-subunit kinase, PEK, involved in translational control', *Mol Cell Biol*,
1250 18: 7499-509.
1251 Sidrauski, C., D. Acosta-Alvear, A. Khoutorsky, P. Vedantham, B. R. Hearn, H. Li, K.
1252 Gamache, C. M. Gallagher, K. K. Ang, C. Wilson, V. Okreglak, A. Ashkenazi, B.
1253 Hann, K. Nader, M. R. Arkin, A. R. Renslo, N. Sonenberg, and P. Walter. 2013.
1254 'Pharmacological brake-release of mRNA translation enhances cognitive
1255 memory', *Elife*, 2: e00498.
1256 Sidrauski, C., J. C. Tsai, M. Kampmann, B. R. Hearn, P. Vedantham, P. Jaishankar, M.
1257 Sokabe, A. S. Mendez, B. W. Newton, E. L. Tang, E. Verschueren, J. R. Johnson,
1258 N. J. Krogan, C. S. Fraser, J. S. Weissman, A. R. Renslo, and P. Walter. 2015.
1259 'Pharmacological dimerization and activation of the exchange factor eIF2B
1260 antagonizes the integrated stress response', *Elife*, 4: e07314.
1261 Siekierka, J., L. Mauser, and S. Ochoa. 1982. 'Mechanism of polypeptide chain
1262 initiation in eukaryotes and its control by phosphorylation of the alpha
1263 subunit of initiation factor 2', *Proc Natl Acad Sci U S A*, 79: 2537-40.
1264 Tsai, J. C., L. E. Miller-Vedam, A. A. Anand, P. Jaishankar, H. C. Nguyen, A. R. Renslo, A.
1265 Frost, and P. Walter. 2018. 'Structure of the nucleotide exchange factor eIF2B
1266 reveals mechanism of memory-enhancing molecule', *Science*, 359: eaaq0939.
1267 van der Knaap, M. S., P. A. Leegwater, A. A. Könst, A. Visser, S. Naidu, C. B. Oudejans,
1268 R. B. Schutgens, and J. C. Pronk. 2002. 'Mutations in each of the five subunits
1269 of translation initiation factor eIF2B can cause leukoencephalopathy with
1270 vanishing white matter', *Ann Neurol*, 51: 264-70.
1271 Vattem, K. M., and R. C. Wek. 2004. 'Reinitiation involving upstream ORFs regulates
1272 ATF4 mRNA translation in mammalian cells', *Proc Natl Acad Sci U S A*, 101:
1273 11269-74.
1274 Welsh, G. I., and C. G. Proud. 1993. 'Glycogen synthase kinase-3 is rapidly inactivated
1275 in response to insulin and phosphorylates eukaryotic initiation factor eIF-
1276 2B', *Biochem J*, 294: 625-9.
1277 Wong, Y. L., L. LeBon, R. Edalji, H. B. Lim, C. Sun, and C. Sidrauski. 2018. 'The small
1278 molecule ISRIB rescues the stability and activity of Vanishing White Matter
1279 Disease eIF2B mutant complexes', *Elife*, 7: e32733.

1280 Wortham, N. C., M. Martinez, Y. Gordiyenko, C. V. Robinson, and C. G. Proud. 2014.
1281 'Analysis of the subunit organization of the eIF2B complex reveals new
1282 insights into its structure and regulation', *Faseb j*, 28: 2225-37.
1283 Wortham, N. C., J. D. Stewart, S. Harris, M. J. Coldwell, and C. G. Proud. 2016.
1284 'Stoichiometry of the eIF2B complex is maintained by mutual stabilization of
1285 subunits', *Biochem J*, 473: 571-80.
1286 Zhang, K. 2016. 'Gctf: Real-time CTF determination and correction', *J Struct Biol*, 193:
1287 1-12.
1288 Zheng, S. Q., E. Palovcak, J. P. Armache, K. A. Verba, Y. Cheng, and D. A. Agard. 2017.
1289 'MotionCor2: anisotropic correction of beam-induced motion for improved
1290 cryo-electron microscopy', *Nat Methods*, 14: 331-32.
1291 Zyryanova, A. F., K. Kashiwagi, C. Rato, H. P. Harding, A. Crespillo-Casado, L. A.
1292 Perera, A. Sakamoto, M. Nishimoto, M. Yonemochi, M. Shirouzu, T. Ito, and D.
1293 Ron. 2021. 'ISRIB Blunts the Integrated Stress Response by Allosterically
1294 Antagonising the Inhibitory Effect of Phosphorylated eIF2 on eIF2B', *Mol Cell*,
1295 81: 88-103.e6.
1296 Zyryanova, A. F., F. Weis, A. Faille, A. A. Alard, A. Crespillo-Casado, Y. Sekine, H. P.
1297 Harding, F. Allen, L. Parts, C. Fromont, P. M. Fischer, A. J. Warren, and D. Ron.
1298 2018. 'Binding of ISRIB reveals a regulatory site in the nucleotide exchange
1299 factor eIF2B', *Science*, 359: 1533-36.
1300